

---

# Design and Fabrication of Optically Resonant Vanadium Dioxide Nanocylinders

---

*Author:*  
Hollie MARKS  
13277103

*Daily Supervisor:*  
Nika VAN NIELEN

*Supervisor & First Examiner:*  
Prof. Dr. Albert POLMAN

*Second Examiner:*  
Dr. Jorik VAN DE GROEP

November, 2022  
60 ECTS  
September, 2021 - November, 2022



Photonic Materials Group  
AMOLF

# *Abstract*

## **Design and Fabrication of Optically Resonant Vanadium Dioxide Nanocylinders**

by Hollie MARKS

Vanadium dioxide ( $\text{VO}_2$ ) displays an ultrafast, reversible semiconductor-metal- transition (SMT) at an accessible critical temperature ( $T_C = 67^\circ\text{C}$ ), which results in drastic modulation of its opto-electronic properties. Exploitation of this phase switching is of great interest for actively tunable nanophotonics, but the sensitivity of  $\text{VO}_2$ 's SMT characteristics to a number of fabrication parameters has restricted its widespread integration. Furthermore, the underlying physics explaining this phase transition is complicated by the simultaneous structural change from monoclinic to rutile that accompanies the SMT. Thus there is widespread interest in improvements to fabrication processes and characterisation of the phase transition in  $\text{VO}_2$ . In this work, we present an optimisation approach for the design and fabrication of a single  $\text{VO}_2$  nanocylinder system which displays optical resonance switching in the visible. We focus specifically on a sample design for novel characterisation of the temporal dynamics of the SMT, proposing pump-probe cathodoluminescence spectroscopy (PP-CL) as a promising technique to examine the phase transition in high spatial and temporal resolution. Finite-difference-time-domain simulations are used to examine the potential of dielectric resonance switching in  $\text{VO}_2$  for phase transition investigation, and the geometric tunability of the resonators is exploited to optimise a design for PP-CL. We then provide a comprehensive investigation into a two-step fabrication process for  $\text{VO}_2$  thin films based on low-temperature electron beam physical vapour deposition and high-temperature annealing, using Rutherford backscattering spectrometry and X-ray diffraction analysis to demonstrate the achievement of highly stoichiometric and crystalline films. Focused ion beam milling of optimised  $\text{VO}_2$  thin films is shown to be an appropriate method for post-deposition nanopatterning, and we present cathodoluminescence measurements which demonstrate the successful exhibition of geometric resonances within a number of  $\text{VO}_2$  nanostructures. We conclude that there is a wealth of potential of this simple design to probe underlying questions about the SMT of  $\text{VO}_2$  while investigating opportunities for novel functionality. The thorough examination of material and geometric influences in this work lays the foundation for further optimisation of the design and fabrication of  $\text{VO}_2$  systems, enabling time-resolved measurements of the SMT with PP-CL. This presents a promising opportunity to contribute to the ongoing research to better understand the underlying transition mechanisms of this complex material.

# Contents

<b>Abstract</b>	<b>i</b>
<b>1 Introduction</b>	<b>1</b>
1.1 Outline of Thesis	2
<b>2 Phase Switching of Vanadium Dioxide</b>	<b>4</b>
2.1 Phase Transition in VO <sub>2</sub>	4
2.1.1 Semiconductor-Metal-Transition	4
2.1.2 Phase Transition Mechanisms and Debate	6
2.2 Optical Resonance Switching	7
2.2.1 Resonant Light-Matter Interactions	7
2.2.2 Dielectric Resonance Switching	8
<b>3 System Design and Optimisation</b>	<b>10</b>
3.1 Pump-Probe Cathodoluminescence Spectroscopy	10
3.1.1 Design Considerations	11
3.2 Optimisation of Sample Design	11
3.2.1 FDTD Simulations	11
3.2.2 Substrate Choice: Si or SiO <sub>2</sub>	12
3.2.3 Particle Geometry: Height	13
3.2.4 Particle Geometry: Diameter	15
3.3 Conclusions and Outlook	16
<b>4 Vanadium Dioxide Thin Film Fabrication</b>	<b>17</b>
4.1 Fabrication of VO <sub>2</sub> in Literature	17
4.1.1 Growth of Stoichiometric VO <sub>2</sub>	17
4.1.2 Impact of Fabrication on SMT	20
4.2 Methods	22
4.2.1 Sample Fabrication	22
4.2.2 Sample Characterisation	23
4.3 Comparison of Demonstrative Samples	24
4.3.1 Stoichiometry	25
4.3.2 Crystallinity	26
4.3.3 Morphology	28
4.3.4 Summary	30
4.4 Additional Findings	30
4.5 Conclusions and Outlook	33
<b>5 Nanocylinder Fabrication and Characterisation</b>	<b>34</b>
5.1 Focused Ion Beam Milling	34
5.2 Cathodoluminescence Measurements	35
5.2.1 Comparison to Simulation	38

5.3	Improved Milling Approach . . . . .	39
5.4	Conclusions and Outlook . . . . .	40
<b>6</b>	<b>Conclusions &amp; Outlook</b>	<b>41</b>
6.1	Outlook . . . . .	41
	<b>Acknowledgements</b>	<b>43</b>
<b>A</b>	<b>Additional Cathodoluminescence Intensity Maps</b>	<b>44</b>
	<b>Bibliography</b>	<b>45</b>

## Chapter 1

# Introduction

Nanophotonics has revolutionised our control of light beyond the diffraction limit, enabling a multitude of important technologies. However, as powerful as the nanophotonics toolbox has proven to be, the majority of optical devices are still static. An extra degree of freedom can be achieved via the introduction of dynamically tunable photonic components into such devices. Phase change materials (PCMs) have received significant attention in recent years for exactly this purpose: rather than a (conventional) fixed optical response, the properties of PCM components can be actively modified by exploiting their phase transition. A number of PCMs display fast, reversible transitions that can be triggered by diverse stimuli such as optical, thermal, or electrical excitation [1]. This can induce drastic changes to the material's optical and electronic properties, allowing functional control of characteristics such as optical transmittance, reflectance or electrical resistivity. A range of existing applications utilise this modulation such as sensing devices [2] and memory storage technology [3].

Vanadium dioxide ( $\text{VO}_2$ ) is a PCM of widespread interest, which displays an ultrafast, reversible semiconductor-metal-transition (SMT) at  $67^\circ\text{C}$  (340K) alongside a crystallographic-phase-transition (CPT) from a monoclinic to rutile structure [4]. The corresponding changes in its electrical conductivity were discovered in 1959, demonstrating three orders of magnitude difference across the SMT [5]. Subsequently, large modulation was also reported for the optical transmittance [6], with  $\text{VO}_2$  almost transparent to infrared (IR) radiation in its low-temperature state, but reflective and opaque in its high-temperature state. This optical and electrical modulation, combined with the accessible transition temperature and range of possible stimuli [7], makes  $\text{VO}_2$  one of the most widely discussed PCMs for opto-electronic applications. One such example is thermochromic coatings for energy-efficient 'smart' windows: elemental doping of  $\text{VO}_2$  enables control over the critical temperature, and the subsequent temperature-dependent transmission can provide autonomous temperature regulation, functional in both hot and cold environments [8].

The exploitation of such phase transitions offers many opportunities for more complex photonic systems. The ability to tune the optical properties of a device without the need for conventional optics enables increased integration and miniaturisation of all-optical systems [9], and the potential of reconfigurable nanophotonic design is similarly broad [10]. The use of unpatterned  $\text{VO}_2$  thin films for tunable metamaterials has been investigated for some years, for example, within hybrid systems made up of  $\text{VO}_2$  thin films with split ring resonators (SRRs) [11, 12]. In these devices, triggering the SMT in the thin films causes significant changes to the optical response of the SRRs, enabling tuning of the resonant frequencies. Furthermore, intermediate

states across the SMT of  $\text{VO}_2$  cause metallic and semiconducting phases to coexist, creating intrinsic spatial variations in permittivity [13]. These variations can be engineered during fabrication such that upon external excitation, thin film  $\text{VO}_2$  can form components such as perfect absorbers [14] and active optical metasurfaces [15].

In addition to the use of unpatterned thin film PCMs to modify photonic devices, there is growing interest in the dual exploitation of a material's phase transition and resonant nanophotonic effects. The drastic modulation of a material's optical properties across the SMT triggers significant changes to the resonances excited, making nanopatterned PCM components highly promising for switchable nanophotonic functionality [13].  $\text{VO}_2$  is again of much interest for these 'resonance switching' systems, with previous work predominantly focused on  $\text{VO}_2$  resonators for plasmonic-dielectric switching in the IR [16, 17]. However, more recently it was shown that  $\text{VO}_2$  could be a promising candidate for all-dielectric, tunable metasurface design [18]. Opportunities for low-loss (dielectric) alternatives to plasmonic resonators are growing [19], and the additional SMT functionality of  $\text{VO}_2$  presents it as a highly interesting material for reconfigurable dielectric nanophotonics.

There are a number of limitations to the performance and fabrication of nanopatterned  $\text{VO}_2$  components. In particular, the highly sensitive material growth [20] and resulting variation in SMT modulation [21] are major challenges to be overcome in order to facilitate  $\text{VO}_2$  integration into optical devices. Simultaneously, despite many years of investigation, the underlying mechanisms driving the phase transition are not fully understood, and are still widely debated [22]. Thus there is widespread motivation for increased research into this material: practical methods for improved fabrication and modulation control, and theoretical and experimental research to better understand the complex physical phenomena of such a system.

Dielectric and/or plasmonic resonances within a single  $\text{VO}_2$  nanocylinder can be exploited to investigate fabrication methods and modulation performance through optical resonance switching. The same system could also be used to examine the time dynamics of the phase transition, expanding the literature on the nature of the interacting mechanisms driving the phase transition. This work presents the design and fabrication of a simple, single-nanocylinder system from which a range of investigations could be based. One such technique of interest is pump-probe cathodoluminescence spectroscopy (PP-CL), a novel characterisation method which combines the high spatial resolution of electron microscopy with the ultrafast temporal resolution of pump-probe measurements [23]. It is with PP-CL in mind that we optimise the sample design and fabrication in this work, exploring a new way to study the phase transition dynamics of  $\text{VO}_2$  with high resolution in both space and time.

## 1.1 Outline of Thesis

This thesis presents a comprehensive study into sample design and fabrication of  $\text{VO}_2$  nanostructures for the investigation of optical resonance switching. In particular, the sensitivity of  $\text{VO}_2$  fabrication is explored, and the complex interaction between material (optical) properties and geometric design is considered. We focus specifically on opportunities for novel characterisation of the temporal dynamics of the phase transition in  $\text{VO}_2$ .

In Chapter 2, the phase switching of  $\text{VO}_2$  is discussed. We present the highly debated mechanisms underlying the semiconductor-metal-transition, and detail the opportunities for dielectric resonance switching within  $\text{VO}_2$  nanostructures. In Chapter 3, we introduce the technique of pump-probe cathodoluminescence spectroscopy (PP-CL) and use finite-difference-time-domain (FDTD) simulations to optimise a single-nanocylinder-on-substrate design appropriate for this technique. Chapter 4 considers the fabrication of  $\text{VO}_2$  thin films, starting with a literature review of the complexities of  $\text{VO}_2$  growth. This is followed by the optimisation of a two-step  $\text{VO}_2$  thin film fabrication approach based on electron-beam physical vapour deposition and high-temperature annealing. In Chapter 5, optimised  $\text{VO}_2$  thin films are patterned via focused ion beam milling. Cathodoluminescence measurements are presented to examine these structures, and FDTD simulations are used to qualitatively discuss further optimisation for PP-CL investigation. Finally, Chapter 6 concludes the findings of this work and details the future outlook, including the potential for time-resolved measurements based on the design in this thesis.

## Chapter 2

# Phase Switching of Vanadium Dioxide

*VO<sub>2</sub> has long been considered an interesting material due to its phase change properties. Its ultrafast phase transition at 67°C from semiconducting to metallic is accompanied by a structural change from monoclinic to rutile. As the material transitions, its optical and electronic properties change significantly, making VO<sub>2</sub> a promising material for a wealth of sensing and switching applications. However, there are a number of unanswered questions regarding the nature of this transition. In this section we will present the theoretical background to the phase transition of VO<sub>2</sub> and discuss the ongoing debate regarding the underlying transition mechanisms. We then examine the emergence of resonances within VO<sub>2</sub> nanostructures, with a focus on dielectric resonance switching in the visible.*

### 2.1 Phase Transition in VO<sub>2</sub>

The widespread interest in the phase transition of VO<sub>2</sub> is two-fold. Firstly, the potential of this phase transition for complex functionality is enormous: the strong opto-electronic modulation, ultrafast timescales and accessible transition temperature make VO<sub>2</sub> one of the most popular materials for phase change applications. Secondly, the complicated underlying physics explaining VO<sub>2</sub>'s phase transition is fascinating and controversial: the SMT in VO<sub>2</sub> can be explained by both electronic and structural mechanisms. Subsequently, there is much debate over the coupling of these transition mechanisms, driving intense theoretical and experimental research. In this section we examine the practical and fundamental aspects of this phase change, and investigate why VO<sub>2</sub> attracts such significant attention from theoretical and applied physicists alike.

#### 2.1.1 Semiconductor-Metal-Transition

Since the first reports of a phase transition in VO<sub>2</sub> by Morin in 1959 [5], the vanadium oxide system, in particular VO<sub>2</sub>, has been extensively studied. This transition in VO<sub>2</sub> is commonly referred to as either a metal-insulator-transition (MIT) or a semiconductor-metal-transition (SMT). In this work, we refer to the SMT, considering the relatively small bandgap ( $E_g = 0.7$  eV) exhibited in the material's insulating phase [24]. Figure 2.1 demonstrates the temperature dependent modulation of electrical resistivity and optical transmittance in VO<sub>2</sub> as it experiences the SMT [6]. Note the sharp transition and hysteresis width seen in both optical and electronic data.

This ultrafast transition occurs at an accessible critical temperature ( $T_C = 67^\circ\text{C}$ ), and is highly reversible, showing minimal degradation under more than  $10^8$  switching



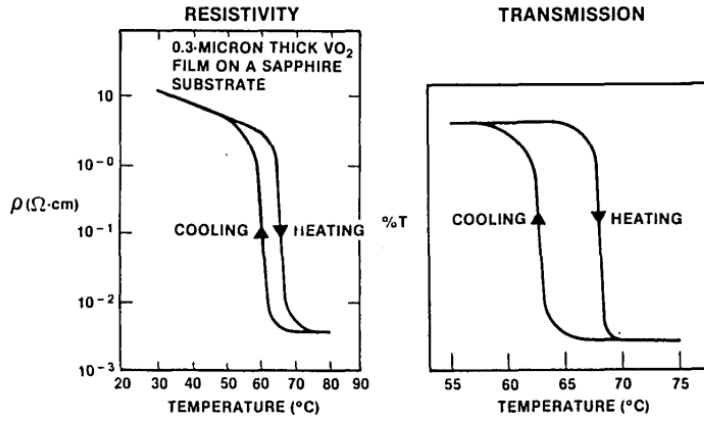


FIGURE 2.1: Temperature dependent optical and electronic switching in thin film  $\text{VO}_2$ . Figure from [6].

cycles [25]. Several other oxides display similar phase transitions, as seen in Figure 2.2, however none with  $T_C$  so close to room temperature. Furthermore, the transition temperature is tunable via elemental doping, with W and Mo ions shown to reduce  $T_C$  [26] and low-valence metal ions such as Cr and Al shown to increase it [27, 28]. Alternative modulation strategies include electrical, via Joule heating [29] or electric field gating [30]; optical, via laser pulse excitation [31]; strain, via substrate lattice mismatch [32]; and chemical, via gradient H-doping [33]. These properties combine to make a functional material that can be used for a wealth of highly-sensitive applications that require a strong, fast and reversible response to external triggers.

There are, however, a number of limitations to the synthesis of  $\text{VO}_2$  for such applications. Most significantly, there is a lack of consistency with regard to material fabrication and the resulting opto-electronic modulation, which is discussed in more detail in Section 4.1. Extensive work has been done to improve fabrication methods for control of the SMT modulation [35, 20]. Despite this, the lack of clarity regarding the underlying SMT mechanisms remains a significant constraint: better understanding of the modulation triggers should enable improved fabrication strategies for practical applications [22]. Practical developments in  $\text{VO}_2$  synthesis have furthered our fundamental understanding, for example, via investigation of the formation of metastable phases [36]. Similarly, improved understanding of the underlying transition mechanisms has presented opportunities for novel modulation strategies [32, 33]. Thus there is a strong connection between the ongoing theoretical research and extensive practical interest in  $\text{VO}_2$ , encouraging continued efforts to bridge between them.

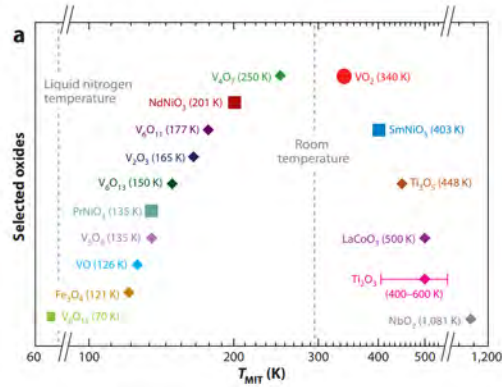


FIGURE 2.2: Metal-insulator-transition (MIT) temperatures for a number of oxides in bulk crystal form. Figure from [34].

### 2.1.2 Phase Transition Mechanisms and Debate

$\text{VO}_2$ , like many other transition metal oxides, is a strongly correlated electron material that is not well described by traditional solid-state models due to strong electron-electron interaction [37]. More specifically,  $\text{VO}_2$  is a typical example of a Mott insulator, a class of materials predicted to conduct electricity according to conventional band theory, but which actually exhibit insulating properties at low temperature and experience a transition from insulator to metal at some critical temperature [38]. Simultaneous to this transition (from now on, referred to as the SMT),  $\text{VO}_2$  experiences a structural change from monoclinic to rutile. It is suggested that this crystallographic-phase-transition (CPT) causes a distortion of the  $\text{VO}_2$  lattice, which in turn modifies the band structure, triggering the observed transition from insulator to metal [24]. Thus there are two explanations for the SMT, which have been extensively investigated with the aim of determining the dominant mechanism. A full discussion of the ongoing debate is outside the scope of this work, but the underlying question is whether the phase transition seen in  $\text{VO}_2$  is driven by lattice effects or electron interactions, or some combination of the two.

The failure of traditional band theory, which is widely successful in predicting the electronic behaviour of solids, to describe the low-temperature, insulating properties of  $\text{VO}_2$  and other correlated materials is well-established [37]. Due to its partly-filled d-electron band,  $\text{VO}_2$  should behave as a metal, but is instead semiconducting below  $T_C$ . This failure is attributed to the single-particle approximation, which assumes an electron moves freely within the effective potential of the surrounding ions and electrons. In reality, correlation effects within the narrow energy band of the d-orbital push the electron charge density closer to the lattice ions. This causes the localisation of electrons to specific atoms, thereby preventing conduction, and explaining the insulating properties seen in low-temperature  $\text{VO}_2$ . In typical Mott insulators, an MIT occurs when external triggers such as thermal or optical excitation provide sufficient energy to delocalise these electrons, allowing conduction of free charge carriers. This transition mechanism driven by electron-electron interactions is known as the Mott-Hubbard model, and is one of the widely proposed mechanisms driving the SMT in  $\text{VO}_2$  [39].

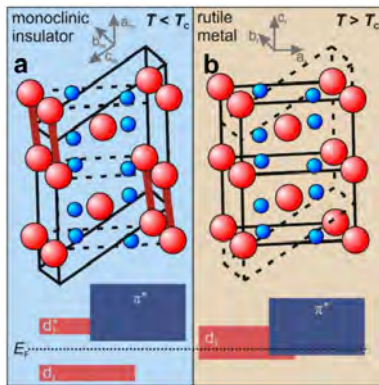


FIGURE 2.3: Crystal and electronic band structure of  $\text{VO}_2$  in its (a) monoclinic, insulating state and (b) rutile, metallic state. Figure from [40].

A second driving mechanism is suggested due to the simultaneous CPT that occurs in  $\text{VO}_2$ : the SMT is accompanied by a structural transition from low-temperature monoclinic (space group  $P2_1/c$ , cell parameters:  $a = 0.575\text{nm}$ ,  $b = 0.452\text{nm}$ ,  $c = 0.538\text{nm}$ ,  $\beta = 122.6^\circ$ ) known as the phase  $\text{VO}_2(\text{M})$ , to high-temperature rutile (space group  $P4_2/mnm$ , cell parameters:  $a = b = 0.455\text{nm}$ ,  $c = 0.286\text{nm}$ ), known as  $\text{VO}_2(\text{R})$  [22]. The crystal structures and corresponding electronic band structures for these two phases are shown in Figure 2.3 [40]. Based on Peierls' theoretical model of a quasi-1D conductor which is unstable at low temperatures due to electron-lattice interactions [41], Goodenough suggested that the lattice distortion caused by the CPT is the trigger of the SMT [24]. Above  $T_C$ , the rutile  $\text{VO}_2$  phase

exhibits equal spacing between nearest V-V atoms, in a highly symmetric formation. This symmetry is broken during the change to a monoclinic structure, whereby dimerisation of the V-V bonds leads to a zigzag configuration with low symmetry and alternating short and long V - V bonds. This lattice deformation is proposed to change the ionic potential in the material, inducing orbital division and leading to the formation of a band gap. Thus a structural transition from rutile VO<sub>2</sub> to monoclinic VO<sub>2</sub> could also be the trigger for the SMT, explaining the unexpected insulating properties at low temperatures.

There is a range of literature suggesting that neither the Peierls nor the Mott-Hubbard mechanisms can explain the SMT in VO<sub>2</sub> alone [42, 43], but there are a number of remaining questions. In particular, the existence of intermediate phases (M2, M3, T) and the size of the bandgap pose challenges to both perspectives [22]. Recent focus has thus been on the coupling of the two mechanisms, with suggestions of both Mott-assisted Peierls or Peierls-assisted Mott mechanisms. A range of in-situ techniques have been utilised to examine the SMT in VO<sub>2</sub> and shed light on the interaction of the mechanisms. For example, evidence of the structural and electronic components occurring at distinct temperature scales led to the discovery of a metal-like monoclinic phase [44] which suggests the two transitions can indeed be distinguished. In addition, time-resolved pump-probe experiments have shown orbital rearrangement upon excitation that is insufficient to suppress the low-temperature lattice distortion, suggesting the structural deformation requires stronger excitation than the electronic trigger [45].

Deconstructing the interactions between the electronic and crystal structure and the orbital arrangement of VO<sub>2</sub> provides opportunities to better understand complex transitions in other correlated materials. In addition, improved understanding of the SMT mechanism is likely to contribute to better modulation control to allow high-performance and widespread VO<sub>2</sub> devices. A combination of theoretical research and experimental investigation has been integral to the current understanding, and novel characterisation of the transition dynamics is key to continue this further.

## 2.2 Optical Resonance Switching

Resonant light-matter interactions pose vast and unique possibilities for the manipulation of light at the nanoscale. In recent years, there has been particular interest in geometric resonances within dielectric nanostructures, due to their promisingly low losses and ability to support a range of electric and magnetic modes [19]. Furthermore, the excitation of resonances within switchable materials such as VO<sub>2</sub> poses exciting opportunities for tunable functionality [46]. In this section, the underlying interactions between light and matter will be presented, and dielectric-dielectric resonance switching in VO<sub>2</sub> nanostructures discussed.

### 2.2.1 Resonant Light-Matter Interactions

When light interacts with matter, discrete electric charges within the material oscillate as they experience the electric component of the incident electromagnetic (EM) radiation [47]. The oscillating charges can then reradiate EM energy, a process known as scattering. Alternatively, incident energy can be transformed into thermal radiation, referred to as absorption. The interaction of EM radiation with a given medium is defined by the complex refractive index,  $n = n + i\kappa$ ; the parallel to this

term is the complex dielectric function,  $\epsilon = \epsilon_1 + i\epsilon_2$ , which describes the response of a medium upon EM illumination.

The scattering properties of a structure are also highly dependent on its geometry. In particular, in the regime concerning (sub)wavelength scale structures, optical resonances can occur which lead to strong enhancement of light-matter interactions [48]. These scattering resonances can be seen in both metallic and dielectric structures of sufficiently small size (hundreds of nm for resonances in the visible). In metallic nanostructures, delocalised conduction band electrons are free to oscillate upon EM illumination, under the condition that the real part of the permittivity ( $\epsilon_1$ ) is negative. When driven at a metallic nanoparticle's natural frequency, this phenomenon is known as a localised surface plasmon resonance (LSPR), and is confined to the surface of the nanoparticle [49]. LSPRs suffer from resonance broadening due to the high Ohmic losses intrinsic to metals.

In contrast, dielectric nanoparticles have considerably lower losses. The localisation of electrons supports displacement current loops, as opposed to the actual current loops present in metallic structures [48]. This results in low absorption losses for these geometric resonances, enabling the confinement of light within the nanoparticle in well-defined spatial modes. In spherical particles, these are referred to as Mie resonances, which occur at the condition  $\lambda = nd$  (where  $d$  is the dimension of the particle) and were described analytically by Gustav Mie [50]. For non-spherical structures which exhibit similar resonant effects, an analytical description is not possible, but numerical methods such as finite-difference-time-domain simulations offer an opportunity to understand this Mie-like behaviour. The low-losses of Mie-like resonances make them sharper than plasmonic resonances, and the modal field distribution within the structures offers a range of interesting functionalities [51].

### 2.2.2 Dielectric Resonance Switching

The intrinsic material losses of plasmonic resonators significantly restrict their scattering efficiencies. In contrast, dielectric resonators offer large scattering cross-sections with low losses, promising high-efficiency interactions that can outperform plasmonics [19, 52]. Furthermore, dielectric nanoparticles can support a range of optical resonances via the interaction of electric and magnetic modes, which are tunable by changing the particle material and geometry [51]. Nanopatterned phase change materials (PCMs) provide a promising platform for switchable nanophotonics [13, 46]. As the material transitions, the modulation of optical properties induces drastic changes to the supported resonances. The subsequent ability to tune and control resonant light interactions in two distinct ways on a single device promises a wealth of applications. VO<sub>2</sub> has been widely proposed as an intriguing system for this emerging field.

The majority of work to demonstrate the use of VO<sub>2</sub> for reconfigurable nanophotonics has focused on dielectric-plasmonic switching in the (near-)infrared ((N)IR) spectral range [16, 17]. However, recent work by Kepic *et al.* demonstrated alternate dielectric-dielectric resonance switching of Mie-like resonances in the visible [18]. Single nanocylinders and nanocylinder arrays of VO<sub>2</sub> on silica substrates were investigated for resonance switching under photoexcitation of the SMT. Dielectric resonances were shown to persist in both low- and high- temperature VO<sub>2</sub>, but the changing optical properties still induced significant switching contrasts between the two phases, demonstrating broad and large modulation depths in scattering (5 - 8



dB) and extinction (1 - 3 dB). Figure 2.4 shows the simulated scattering cross-sections for single VO<sub>2</sub> nanocylinders on a silica substrate ( $h = 200$  nm,  $100$  nm  $< d < 300$  nm) in the (a) low- and (b) high- temperature phases, alongside (c) the complex dielectric function for both phases. Note that in the visible,  $\epsilon_1$  is positive in both the low- and high- temperature phases, and it is only in the NIR that  $\epsilon_1$  drops below zero for the high-temperature phase. Thus, based on the enhancement condition ( $\epsilon_1 < 0$ ), the emergence of plasmonic resonances is restricted to the NIR. This means that in the visible spectral range, both the semiconducting and metallic phases of VO<sub>2</sub> exhibit dielectric scattering, but the change in optical properties ensures that the scattering responses are distinct.

In addition to the large modulation depths, the tunability of resonance spectral position with diameter was demonstrated, enabling modulation enhancement via geometric optimisation [18]. Furthermore, these resonances exhibited sharpening when formed into a nanocylinder array, and were shown to be switchable under continuous-wave illumination. This work suggests VO<sub>2</sub> structures are a promising ‘building block’ for tunable nanophotonics, particularly with an interest in low-loss applications in the visible. Thus VO<sub>2</sub> is highlighted as an exciting material system for ongoing efforts to explore switchable photonic functionality. Furthermore, the large switching contrast between the low- and high-temperature dielectric resonances could be exploited for a number of characterisation techniques, such as time-resolved characterisation of the phase transition, as will be discussed in Section 3.1.

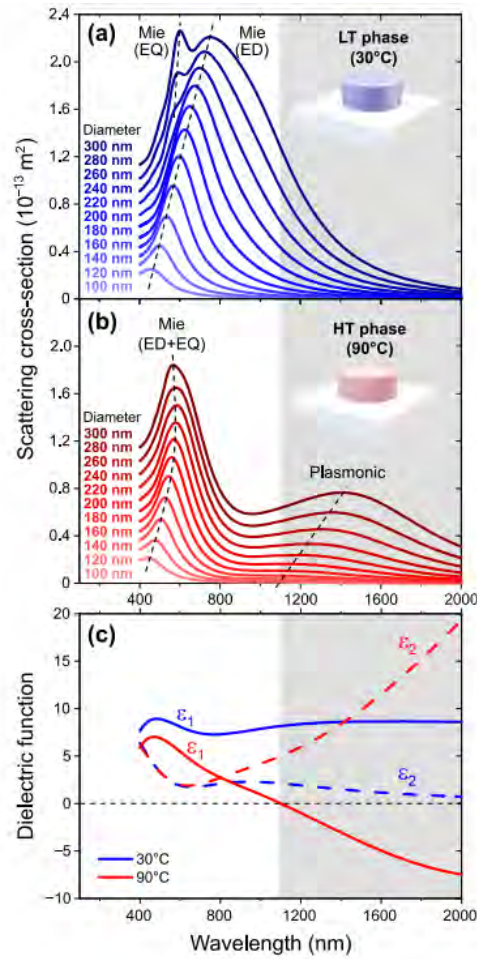


FIGURE 2.4: (a-b) Simulated scattering cross-sections of single VO<sub>2</sub> nanocylinders of  $h = 200$  nm and variable diameter on a fused silica substrate for (a) low-temperature phase and (b) high-temperature phase. The dashed lines show the positions of plasmonic and Mie (electric dipole (ED) and electric quadrupole (EQ)) resonances. The spectral region of plasmonic VO<sub>2</sub> is shaded in grey. (c) Real ( $\epsilon_1$ ) and imaginary ( $\epsilon_2$ ) parts of the dielectric function as extracted from spectroscopic ellipsometry data of a VO<sub>2</sub> thin film of 93 nm thickness on a silicon substrate. Figure from [18].

## Chapter 3

# System Design and Optimisation

*In the previous chapter we have established the complex phase switching of VO<sub>2</sub>, and highlighted ongoing research interests. There is clear motivation for further investigation to bridge the underlying theory and novel photonic applications. For this reason, we focus our attention to opportunities for novel investigation of the switching dynamics of VO<sub>2</sub>. Pump-probe cathodoluminescence (PP-CL) spectroscopy is a promising characterisation technique for examining ultrafast material dynamics with high temporal and spatial resolution. In this chapter, we investigate the geometric design of a VO<sub>2</sub> system which could be used for PP-CL measurements. We consider a system designed to exhibit dielectric switching of Mie-like resonances in the visible, based on previous work that has demonstrated strong and tunable modulation in this spectral range [18]. Finite-difference-time-domain simulations are used to optimise the sample geometry for the purposes of PP-CL, and the effects of substrate index and cylinder geometry on the subsequent switching are discussed in this context.*

### 3.1 Pump-Probe Cathodoluminescence Spectroscopy

Pump-probe techniques have been widely employed for the investigation of the complex SMT of VO<sub>2</sub>, providing estimates of the transition timescale (ranging from femtoseconds to a few picoseconds [53]) and examining the coexistence of the structural and electronic transitions [17, 45, 54]. Previous literature has also investigated reversible phase transitions with ultrafast electron microscopy techniques, enabling spatial and/or temporal investigation of structural transition dynamics [55, 56]. Pump-probe cathodoluminescence (PP-CL) spectroscopy is a similar electron beam based technique that combines high spatial and temporal resolution, but which ultimately measures the optical cathodoluminescence (CL) emission of the studied sample.

CL is the emission of light after material interaction with an electron beam. The use of CL spectroscopy for the study of nanophotonic structures offers a significant advantage to traditional optical techniques due to its high spatial resolution. The diffraction limit of conventional optical sources sets a spatial resolution of a few hundred nanometres [57]. Having smaller wavelengths than light, electron sources can offer sub-angstrom resolution, although this is limited to a few nm by the electron optics within the microscope [58]. The tightly confined electric field of the electron behaves as a broadband source that can excite modes at a range of spectral positions. The combination of this high spatial resolution with the temporal resolution of ultrafast pump-probe techniques lends PP-CL a huge potential for probing complex material dynamics such as the phase transition of VO<sub>2</sub>. Our PP-CL setup consists of an integrated SEM and optical setup, with pulsed electron and laser beams, either

of which can be used as the pump to excite the sample, or the probe to examine the CL response. The temporal delay between the pump and probe can be controlled in order to investigate the resulting dynamics. Further details can be found in [59].

As shown by Kopic *et al.*, single nanocylinders of VO<sub>2</sub> exhibit strong and distinct scattering in both the low- and high- temperature phases in the visible spectral range, with corresponding modulation depths of significant magnitude (see Section 2.2.2) [18]. The spectral response of the nanostructure can thus be seen as an indicator for the phase of the material, and examination of the CL response at various time delays after excitation could enable novel investigation of the temporal dynamics of the phase transition. Furthermore, the high spatial resolution of PP-CL enables the mapping of excited modes within nanostructures. This means that in addition to ultrafast temporal characterisation, this technique could demonstrate how the confinement of light changes as the material switches phase. Thus VO<sub>2</sub> is also an interesting model system to demonstrate the future potential of PP-CL.

### 3.1.1 Design Considerations

Kopic *et al.*'s systematic study of Mie-like resonances in VO<sub>2</sub> provides a basis to optimise a single-nanocylinder-on-substrate design. For PP-CL, there are two additional design parameters to consider:

1. **Silicon substrate:** Due to the coupled nature of photon and electron excitation in the setup, certain samples will exhibit a photoluminescence (PL) signal in addition to the desired CL signal. To enhance the CL signal enough to distinguish it from the background PL, high currents must be used, but this causes limitations to the spatial resolution of measurements. As such, samples with minimal to no PL response are the most promising for high spatial resolution PP-CL spectroscopy. Silicon substrates are therefore much preferred to materials such as quartz (SiO<sub>2</sub>) which exhibits a strong PL response. In addition, the use of Si substrates prevents charging effects due to the electron beam.
2. **Optimised for 600 nm:** The avalanche photo-diodes (APDs) used as single-photon counting detectors in the PP-CL setup (see [59]) have a variable photoelectric conversion sensitivity dependent on wavelength. For optimal sensitivity, wavelengths around 600 nm are desired, and at wavelengths as low as 400 nm or as high as 900 nm there is a drastic decrease in sensitivity of almost one order of magnitude [60]. Optimising the resonance position around 600nm ensures maximum collection of the emitted CL signal.

We thus present finite-difference-time-domain (FDTD) simulations to examine how the substrate material and nanocylinder geometry impact the scattering cross-sections and switching contrasts, in order to optimise a sample design for the purposes of PP-CL measurements. Van de Groep and Polman presented a systematic study of the design of dielectric resonators [51], which is used as a guide for the discussion below.

## 3.2 Optimisation of Sample Design

### 3.2.1 FDTD Simulations

FDTD simulations were carried out using Lumerical Solutions [61]. The simulation design consisted of a semi-infinite substrate (Si or SiO<sub>2</sub>) with a single VO<sub>2</sub> nanocylinder of variable height and diameter. Optical constants for Si and SiO<sub>2</sub> were taken

from Palik [62], and optical constants for both phases of  $\text{VO}_2$  were extracted from the dielectric function data presented by Kepic *et al.*, as seen in Figure 2.4(c) [18]. All simulations were run in three dimensions, using perfectly matched layer (PML) boundary conditions in the  $z$  direction, and anti-symmetric and symmetric boundary conditions in the  $x$  and  $y$  directions respectively.

Plane wave illumination was modelled by the use of a total-field-scattered-field (TFSF) source, which separates the scattered field from the transmitted and reflected fields. We measure the scattering cross-section by placing cross-section analysis monitors outside the TFSF box. The injection axis of the TFSF source was in the  $z$  direction, and the TFSF geometry was varied according to the size of the simulated structures. In addition, convergence testing showed that a mesh size of 2nm was required to ensure artifacts or unphysical effects were avoided. Thus a mesh refinement buffer region was added around the structures.

### 3.2.2 Substrate Choice: Si or $\text{SiO}_2$

The index contrast between a resonator and its substrate has a strong influence on the confinement of the modes. Figure 3.1(a) shows the normalised scattering cross-section ( $Q_{\text{scat}} = \frac{\sigma_{\text{scat}}}{\sigma_{\text{geometric}}}$ ) for a Si resonator of  $d = 100$  nm,  $h = 100$  nm, on a substrate with variable refractive index ( $1 < n_{\text{sub}} < 3.5$ ) [51]. As  $n_{\text{sub}}$  increases, the resonances broaden due to increased radiative losses caused by mode extension into the substrate. Additionally, the spectral overlap of the electric dipole (ED) and magnetic dipole (MD) increases with  $n_{\text{sub}}$ , with the ED mode appearing as a shoulder on the dominant MD mode. These effects demonstrate the significant role of substrate-cylinder coupling on resonance spectra, highlighting the importance of considering substrate index when designing nanoresonators.

The refractive index of Si ( $n = 3.9$ ) is significantly higher than that of  $\text{SiO}_2$  ( $n = 1.5$ ). Thus the scattering cross-sections could change substantially if the  $\text{SiO}_2$  substrate was replaced by Si. To check whether this change in substrate suppresses the desired resonance switching, a range of comparison simulations were run. Figure 3.2

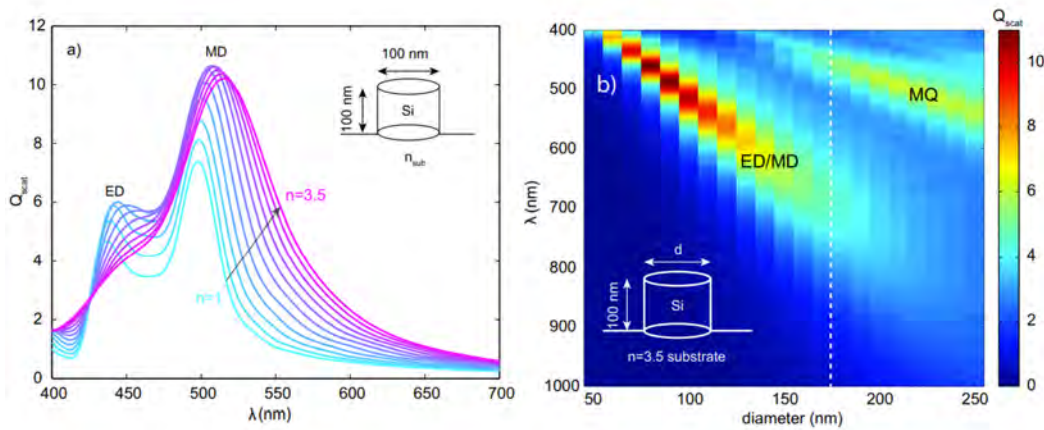


FIGURE 3.1: **(a)**  $Q_{\text{scat}}$  for a single Si cylinder of  $d = 100$  nm,  $h = 100$  nm, on a substrate with changing index  $1 < n < 3.5$ . **(b)**  $Q_{\text{scat}}$  (colourbar) as a function of  $\lambda$  and  $d$  for a single Si cylinder of  $h = 100$  nm,  $50 \text{ nm} < d < 250$  nm, on a substrate with  $n = 3.5$ . Figures from [51].



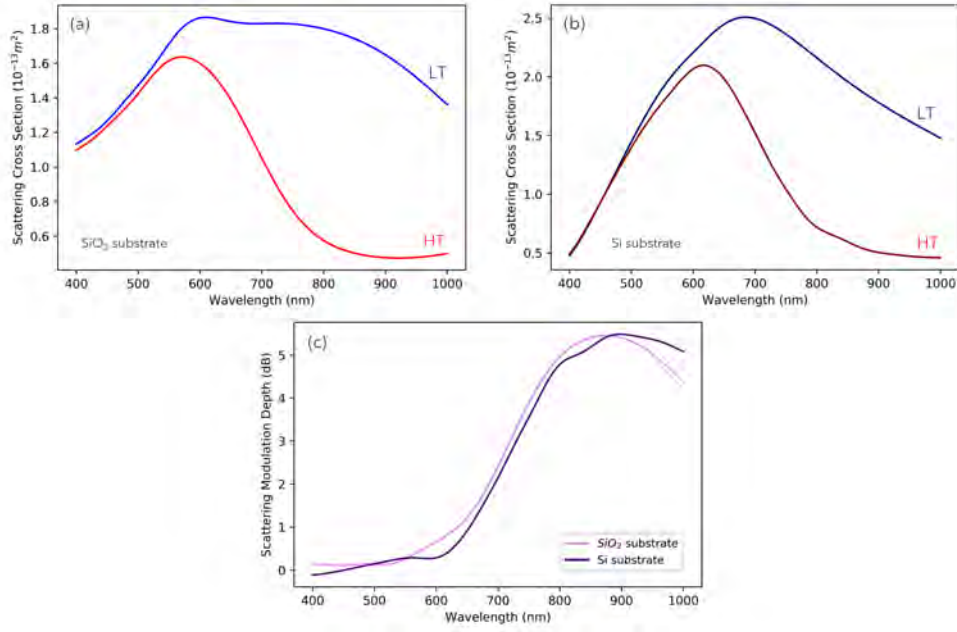


FIGURE 3.2: Simulated scattering cross-sections for both low- (LT) and high- (HT) temperature phases of a single  $\text{VO}_2$  nanocylinder of  $d = 200 \text{ nm}$ ,  $h = 200 \text{ nm}$ , on a (a)  $\text{SiO}_2$  and (b)  $\text{Si}$  substrate. (c) Corresponding scattering modulation depths.

shows the simulated scattering cross-sections for a  $\text{VO}_2$  nanocylinder of  $d = 200 \text{ nm}$ ,  $h = 200 \text{ nm}$ , on an (a)  $\text{SiO}_2$  or (b)  $\text{Si}$  substrate. As described in [51], on the higher index  $\text{Si}$  substrate the resonances appear to broaden, and the modes (identified as the ED and electric quadrupole (EQ) modes in [18]) show increased spectral overlap. Additionally, the scattering cross-section is increased for the cylinder on  $\text{Si}$ , due to an increased local density of states (LDOS) with higher refractive index.

For the purposes of resonance switching measurements, the modulation depth, given by  $\mu = 10 \log(\frac{I_{\text{LT}}}{I_{\text{HT}}})$  [18], must be considered in addition to the scattering cross-section. Figure 3.2(c) shows that the scattering modulation depth for either substrate is comparable. Thus, regardless of the higher radiative losses into the substrate and decreased mode confinement, the use of a  $\text{Si}$  substrate should display appropriate scattering modulation to examine resonance switching of  $\text{VO}_2$  nanocylinders.

### 3.2.3 Particle Geometry: Height

The height of a nanostructure is also highly influential in the subsequent resonance response. In particular, the excitation of the MD mode relies on the sufficient retardation of the electric field within the particle to give the appropriate phase shift required for MD excitation [63]. Therefore, if a cylinder is of insufficient height for this phase shift to occur, the structure will exhibit only electric modes rather than electric and magnetic ones. In addition, red-shifting of resonance peaks is seen with increasing height for  $\text{Si}$  resonators [51].

However, multipole decomposition analysis has demonstrated a weak contribution from magnetic modes to the resonances excited in both the low- and high- temperature phase of  $\text{VO}_2$  [18], as seen in Figures 3.3(a,b). This effect is attributed to the

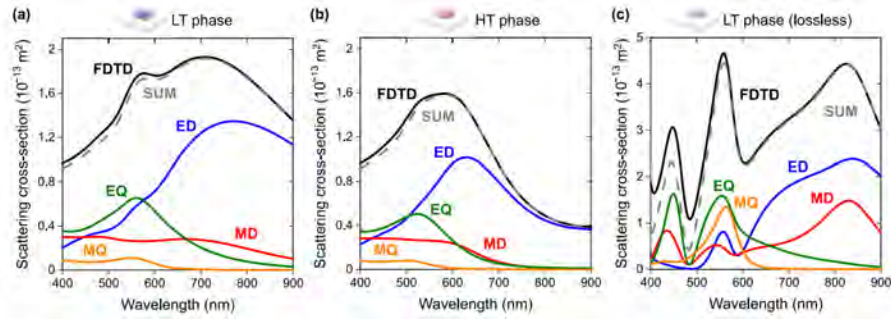


FIGURE 3.3: Multipole scattering decomposition of  $\text{VO}_2$  nanocylinders of  $h = 200$  nm,  $d = 270$  nm, in the (a) low-temperature and (b) high-temperature phase. (c) Multipole decomposition for the same structure with artificially set optical constants, extinction coefficient,  $\kappa = 0$ , and mean (LT) refractive index,  $n = 2.89$ . Figure from [18].

losses in  $\text{VO}_2$  due to its non-zero absorption coefficient. Figure 3.3(c) further demonstrates the key role of loss in enabling the excitation of magnetic modes within  $\text{VO}_2$  nanostructures. The contribution from the magnetic modes is drastically increased for a cylinder with artificially fixed optical constants,  $n = 2.89$  and  $\kappa = 0$ , demonstrating that if losses can be minimised,  $\text{VO}_2$  can be optimised to exhibit both magnetic and electric modes [18].

Thus the effect of varying height in  $\text{VO}_2$  nanocylinders is not directly comparable to that of Si resonators due to the lack of magnetic modes. However, the height still plays a significant role in the spectral position of the excited resonances. Figure 3.4 shows the resonant wavelengths for scattering spectra in both the low- and high-temperature phase for nanocylinders of variable diameter ( $100 \text{ nm} < d < 400 \text{ nm}$ ) and height ( $h = 100 \text{ nm}, 200 \text{ nm}, 300 \text{ nm}$ ). Red-shifting of the peak resonant wavelengths occurs as the height increases. These simulations demonstrate the nanocylinder height most appropriate to achieve resonances at the target wavelength for PP-CL: at  $h = 100 \text{ nm}$ , the resonance spectral positions are below  $600 \text{ nm}$ , and at  $h = 300 \text{ nm}$ , the majority of diameters exhibit resonances at higher wavelengths. Thus we choose a height of  $200 \text{ nm}$  for our structures.

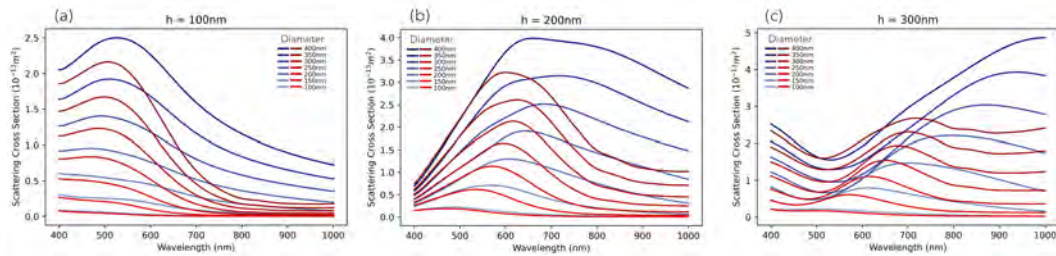


FIGURE 3.4: Simulated scattering cross-sections for low- (blue) and high- (red) temperature  $\text{VO}_2$  nanostructures of variable diameter,  $100 \text{ nm} < d < 400 \text{ nm}$ , and height: (a)  $100 \text{ nm}$  (b)  $200 \text{ nm}$  (c)  $300 \text{ nm}$ .

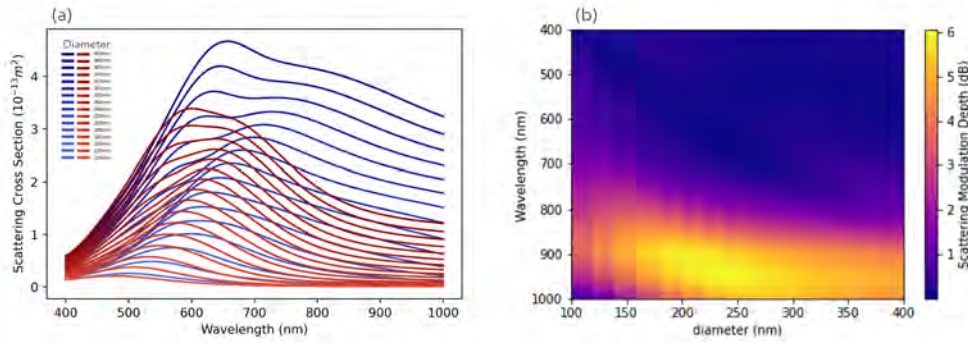


FIGURE 3.5: **(a)** Simulated scattering cross-sections for low- (blue) and high- (red) temperature  $\text{VO}_2$  nanocylinders of  $h = 200$  nm and variable diameter,  $100 \text{ nm} < d < 400 \text{ nm}$ , increasing in 20 nm increments. **(b)** Corresponding scattering modulation depth (colourbar) as a function of  $\lambda$  and  $d$ .

### 3.2.4 Particle Geometry: Diameter

The nanocylinder diameter determines the presence of higher order modes and the spectral spacing between different modes [51]. With height set at 200 nm, we simulate a range of diameters ( $100 \text{ nm} < d < 400 \text{ nm}$ ) in order to investigate the most promising nanocylinder size for PP-CL measurements. Figure 3.5(a) shows the low- and high- temperature scattering cross-sections of these cylinders. Smaller nanocylinders, with diameters below around 200 nm, demonstrate a single peak in the scattering spectra, corresponding to the ED mode. As the diameter increases a second peak emerges, corresponding to the EQ mode (as identified by Kepic *et al.* [18]). This is in agreement with the emergence of higher order modes at sufficiently large diameters seen in Figure 3.1(b), bar the lack of magnetic modes hosted in  $\text{VO}_2$ . In addition, as diameter increases, the resonances are red-shifted and the spectral spacing between the modes increases.

Figure 3.5(b) shows the scattering modulation depth extracted from these simulations. The cylinders exhibit significant scattering modulation that peaks at 6 dB, but this occurs at 900 nm which is outside the optimal range of our APDs. At 550 nm - 650 nm, the maximum modulation is achieved by cylinders of 150 nm diameter, and is approximately 3 dB (see Figure 3.6). This is a factor of two smaller than at higher wavelengths, but still of sufficient magnitude. From Figure 3.5(a), however, it is evident that at such small diameters, the scattering cross-section is low, and the resonances appear broad and weak compared to those at larger diameters. Where  $Q_{\text{scat}}$  is a good indicator of the relative strength of resonances, it is slightly inappropriate to consider for comparison in this case: to ensure that the CL response will be sufficiently high to detect, the *total* scattering signal must be considered in addition to the modulation depth.

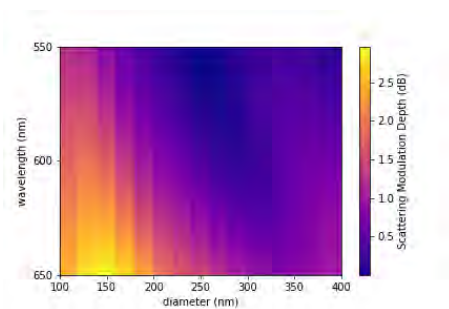


FIGURE 3.6: Simulated scattering modulation depth as a function of  $\lambda$  and  $d$  for the same cylinders as Figure 3.5.

### 3.3 Conclusions and Outlook

Based on the work of Kepic *et al.* [18] and Van de Groep and Polman [51], we have shown that the design of a VO<sub>2</sub> nanocylinder-on-substrate can be modified in order to tune the resonance position, enhance the scattering cross-section, and optimise the scattering modulation depth. Furthermore, this work shows that a single VO<sub>2</sub> nanocylinder could be a suitable system to examine ultrafast phase switching dynamics with PP-CL.

In conclusion, these simulations indicate that there is not one single 'optimised' geometry for this sample. Rather, there are a number of geometric requirements for nanostructures that exhibit resonances at our wavelengths of interest ( $h = 200$  nm), with adequate scattering signal ( $d > 150$  nm) and sufficiently strong scattering modulation ( $d < 300$  nm). To determine the best compromise between optimised scattering signal and modulation depth, it is suggested to fabricate nanocylinders of a range of sizes and investigate their optical response experimentally. Based on the findings of this section, we propose the fabrication of VO<sub>2</sub> nanostructures of  $h = 200$  nm and  $150 \text{ nm} < d < 300 \text{ nm}$ . In the next chapter, we investigate thin film fabrication of VO<sub>2</sub>, for eventual post-deposition patterning.

## Chapter 4

# Vanadium Dioxide Thin Film Fabrication

*Following from the geometric optimisation of VO<sub>2</sub> nanostructures for optical resonance switching, we now present the material fabrication. The complexity and sensitivity of VO<sub>2</sub> growth indicates that post-fabrication patterning of thin films is favourable to pre-deposition patterning methods. In this chapter, the fabrication of stoichiometric, crystalline and homogeneous VO<sub>2</sub> thin films is examined. First, we present how the thermodynamic phase stability, reaction kinetics, and oxidation growth model of VO<sub>2</sub> influence the stoichiometry of vanadium oxide thin films. This is followed by an examination of how crystallinity and morphology affect the SMT characteristics. We then present an investigation into VO<sub>2</sub> thin film growth based on electron-beam physical vapour deposition and post-deposition annealing. Through characterisation via Rutherford backscattering spectroscopy, X-ray diffraction analysis, and scanning electron microscopy, we optimise a fabrication recipe. Furthermore, we investigate the tunability of thin film microstructure by changing annealing parameters, and highlight further considerations for the optimisation of VO<sub>2</sub> thin film fabrication.*

## 4.1 Fabrication of VO<sub>2</sub> in Literature

Due to the number of oxidation states of vanadium, synthesis of single-phase VO<sub>2</sub> thin films requires extensive optimisation. In addition, the sensitivity of the SMT characteristics to material crystallinity and morphology further complicates the process. Much work has been done to improve deposition methods for VO<sub>2</sub> [35, 20], but the process window for this fabrication remains very narrow [64], and extreme sensitivity to a range of deposition parameters is a major limitation [65]. While much literature has focused on single-step, high-temperature, reactive deposition of thin films, the optimisation process is simplified by a two-step approach consisting of room temperature deposition followed by post-deposition annealing [64, 65, 52]. In this section, we present a literature review examining the nature of this material growth and how the deposition process can modify the phase transition, motivating the careful optimisation of a two-step fabrication process.

### 4.1.1 Growth of Stoichiometric VO<sub>2</sub>

#### Phase Stability

The first significant limitation to the simple fabrication of VO<sub>2</sub> thin films is the large number of vanadium oxide phases. When synthesising metal oxides by oxygen annealing, as investigated in this work, the pressure and temperature conditions of the oxidation determine the oxide phases that are stable and likely to form [65, 66]. The



oxidation parameters must therefore be carefully controlled to ensure the desired oxide phase is dominant. There are four single-valence states of vanadium (+2, +3, +4, +5), corresponding to distinct phases VO,  $V_2O_3$ ,  $VO_2$ ,  $V_2O_5$ , in addition to the intermediate, mixed-valence oxides known as the Magneli ( $V_nO_{2n-1}$ ) and Wadsley ( $V_nO_{2n+1}$ ) phases. A number of these vanadium oxides exhibit a SMT, but as seen in Figure 4.1, the majority do not transition at such an accessible temperature as  $VO_2$  [67].

This abundance of oxide phases creates a very narrow window for parameter optimisation. Phase diagrams, which represent the thermodynamic conditions required for the stability of different material phases, demonstrate the ease of oxidation or reduction of a given phase at certain conditions. A simplified phase diagram considering only the single-valence phases of vanadium oxide is presented in Figure 4.2(a) [66]. Known as an Ellingham diagram, this shows the equilibrium energy change of oxidation or reduction ( $\Delta_r G^0$ , left y-axis) and oxygen partial pressure ( $P_{O_2}$ , right y-axis) against temperature, with the black lines indicating the phase boundaries of different vanadium oxides. This highlights the high-temperature and low-pressure conditions required for  $VO_2$  phase stabilisation. For example, the blue markers demonstrate that for a temperature of 500°C, the stable pressure regime for  $VO_2$  is  $10^{-3}$  Pa to  $10^{-14}$  Pa.

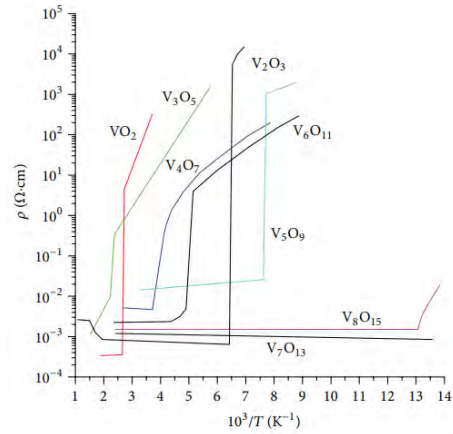


FIGURE 4.1: Resistivity against reciprocal temperature for intermediate (Magneli) phase vanadium oxides. Figure from [67].

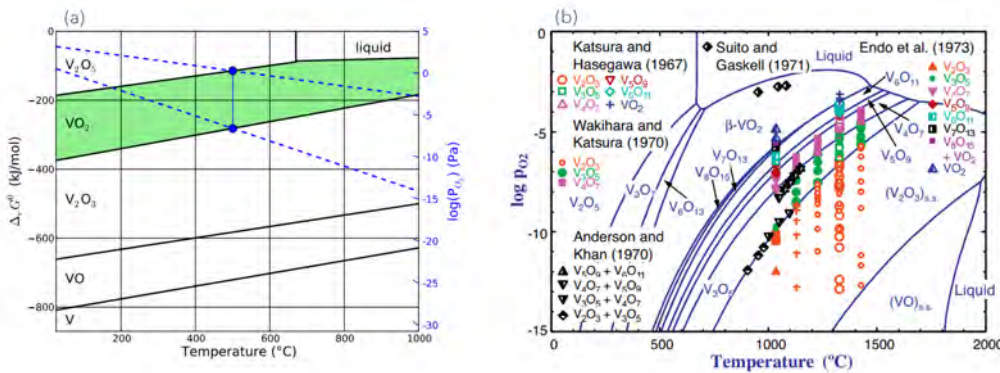


FIGURE 4.2: (a) Ellingham diagram for the single-valence vanadium oxides, showing the equilibrium energy change of a reaction ( $\Delta_r G^0$ ) on the left y-axis and oxygen partial pressure ( $P_{O_2}$ ) on the right y-axis, as a function of temperature. The blue markers indicate the range of  $P_{O_2}$  for which  $VO_2$  is stable at 500°C. Diagram from [66]. (b) Calculated phase diagram for the entire V-O system, showing  $P_{O_2}$  against temperature. Experimental data is also marked. Figures from [68].

In reality, however, the mixed Magneli and Wadsley phases must also be considered. Figure 4.2(b) is a calculated phase diagram of all vanadium oxide states [13], which further shrinks the regime at which  $\text{VO}_2$  is dominant, for example to just  $10^{-4}$  Pa to  $10^{-9}$  Pa at  $500^\circ\text{C}$  [66]. Such low pressure requirements pose practical limitations such as poor flow control in annealing setups [66]. On the other hand,  $\text{VO}_2$  phase stability at higher pressures requires temperatures far above  $500^\circ\text{C}$ , which can cause film degradation and restricts the choice of substrate material [69]. Thus there are significant complications regarding the oxidation of vanadium within the regime where  $\text{VO}_2$  is thermodynamically stable.

### Reaction Kinetics and Growth Mechanism

As explained by Rampelberg, however, the thermodynamic analysis considered in Figure 4.2 does not take the kinetics of the reaction into account [66]. Where thermodynamics describes the equilibrium direction of a reaction, kinetics is concerned with the pathway; thermodynamic considerations describe overall energetics – the products most likely to occur, whereas kinetics describe how these products are formed – the rate of reaction [70]. In many cases, the kinetics are the limiting factor of a reaction rather than the thermodynamic stability of products [71]. In this case, if the rate of vanadium oxidation is well-controlled such that it forms  $\text{VO}_2$  before reaching its stable state, the processing time can be optimised for growth of  $\text{VO}_2$ , even outside of its thermodynamically stable regime.

The Deal-Grove model for metal oxide formation during oxidation finds that oxygen partial pressure is highly influential on the oxide growth rate: during initial growth, the rate increases linearly with oxygen partial pressure, and at later stages the relation becomes parabolic. Additionally, this growth rate is dependent on temperature. The flux of oxygen depends on the effective diffusion coefficient,  $D = \exp(\frac{-E}{kT})$ . As oxygen flux is proportional to oxide growth, the rate of growth increases exponentially with temperature [72]. Literature has shown that the oxidation of vanadium is in agreement with the Deal-Grove model [64, 71, 73], with a rate of growth highly dependent on oxygen partial pressure and temperature.

Figure 4.3 shows in-situ XRD measurements as a V thin film was annealed in air [74]. A characteristic  $\text{VO}_2$  peak appears after a few minutes of oxidation, but minutes later a  $\text{V}_2\text{O}_5$  peak emerges and subsequently the  $\text{VO}_2$  peak disappears. This demonstrates that the reaction kinetics can be exploited to fabricate  $\text{VO}_2$ , as discussed above, highlighting the importance of carefully optimising the annealing time. In addition, there is a significant difference between  $\text{VO}_2$  growth and the growth of oxides such as  $\text{SiO}_2$  [74]. Whereas  $\text{SiO}_2$  grows on top of Si with a sharp Si/ $\text{SiO}_2$  interface, Figure 4.3 shows that during annealing, the V peak quickly disappears as the film reacts with oxygen. This suggests that rather than growth on top of an unoxidized, ‘pure’ vanadium layer with a sharp V/ $\text{VO}_2$  interface, the oxide forms above an oxidised  $\text{VO}_x$  layer. Generally, the highest valence state (the most oxygen-rich oxide) is found at the top, and the lowest valence state (the most oxygen-deficient) at the substrate/thin film interface [64].

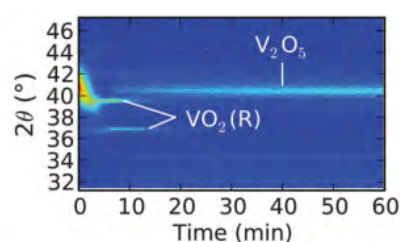


FIGURE 4.3: XRD measurements during oxidation of a V thin film in air at  $480^\circ\text{C}$ . Figure from [74].

Figure 4.4 shows a schematic of the understood vanadium oxide growth mechanism, based on [66]. Initially, an undefined layer of  $\text{VO}_x$  forms (with  $x < 2$ ), followed by the growth of a  $\text{VO}_2$  layer on top. The undefined layer is a graded layer of mixed oxidation states. As the film oxidises further, a complete  $\text{VO}_2$  layer forms by the conversion of the mixed layer to  $\text{VO}_2$ . At  $t_{\text{VO}_2}$ , the time at which this occurs, the reaction kinetics and thermodynamic stability of different oxides are critical: in the  $\text{VO}_2$  stable regime, the oxidation process stops at  $t_{\text{VO}_2}$ , but in a temperature/pressure regime where a different oxide dominates, the oxidation process continues until higher oxidation states form on top of the  $\text{VO}_2$ , and eventually form the complete thin film.

Given the practical limitations of oxidation within the low-pressure, high-temperature regime required for  $\text{VO}_2$  phase stability, control of the reaction rate for careful optimisation of annealing time is a promising approach for thin film fabrication [66]. This still presents a narrow process window, but by using low pressures and/or temperatures to minimise the reaction rate, the sensitivity of this time parameter can be reduced. This manipulation of the reaction rate is an effective way to overcome the stoichiometry issues presented by the complex phase system of vanadium oxides, and is thus the basis for the fabrication methods presented in this work.

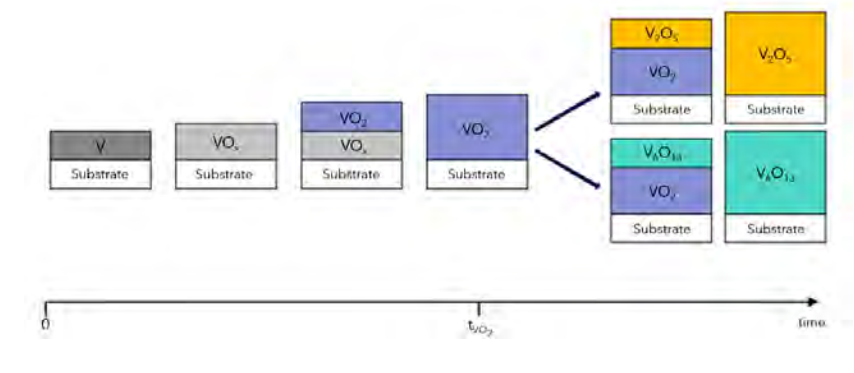


FIGURE 4.4: Schematic of the understood growth mechanism of vanadium thin film oxidation. Figure based on [66].

#### 4.1.2 Impact of Fabrication on SMT

For switching applications or phase transition characterisation,  $\text{VO}_2$  thin films should demonstrate strong modulation of optical and electrical properties across the SMT. Unfortunately, good stoichiometry does not necessarily correlate with this desired phase switching. Whilst oxygen non-stoichiometry is shown to cause a significant reduction of electrical resistivity modulation [75], there are a number of other influences on the SMT characteristics of  $\text{VO}_2$  thin films, in particular their atomic and grain structure. Thus, optimisation attempts should focus not only on obtaining thin films with the appropriate O/V ratio, but also on the crystallinity and morphology.

##### Thin Film Crystallinity

A major consideration to ensure the desired SMT modulation in  $\text{VO}_2$  thin films is the crystallinity of the material. The SMT of interest for this work is exhibited in crystalline, monoclinic  $\text{VO}_2$  as it transforms to a rutile structure. The fabrication of monoclinic  $\text{VO}_2(\text{M})$  is complicated by the existence of a number of polymorphs of  $\text{VO}_2$  such as  $\text{VO}_2(\text{B})$  (monoclinic) and  $\text{VO}_2(\text{A})$  (tetragonal) that have the same stoichiometry as  $\text{VO}_2(\text{M})$  but do not display this transition [20].



Amorphous  $\text{VO}_2$  thin films show strong suppression of SMT modulation when compared to crystalline samples [76]. To avoid this, films can be fabricated by crystalline deposition methods. Reactive pulsed laser deposition [8], radiofrequency magnetron sputtering [77] and reactive electron beam evaporation [78] have been demonstrated to successfully form crystalline  $\text{VO}_2$ , although substrate heating above  $400^\circ\text{C}$  is required in all cases to ensure appropriate crystallinity. These single-step, high-temperature deposition approaches, however, are inconsistent due to the non-uniformity of substrate heating methods [65].

Alternatively,  $\text{O}_2$  annealing of amorphous films is also found to produce crystalline films [76]. This annealing step can serve the purpose of oxidation, crystallisation, or both. During the annealing of both reactive and pure deposited films, a range of  $\text{VO}_2$  crystal structures form depending on the process parameters. Further, different  $\text{VO}_2$  polymorphs are stabilised depending on the gas environment or temperature [35]. Previous work has shown consistent formation of the monoclinic phase of  $\text{VO}_2$  after annealing at  $500^\circ\text{C}$  [79, 80]. For this reason, an annealing temperature of  $500^\circ\text{C}$  is used in this work.

### Thin Film Morphology

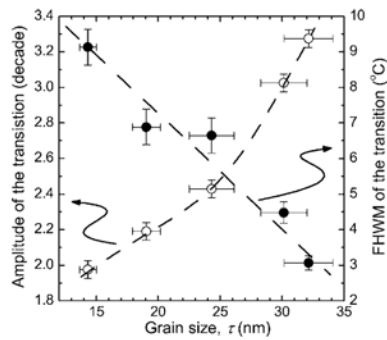


FIGURE 4.5: Amplitude of electrical switching (left y-axis) and sharpness of the SMT (right y-axis) as a function of grain size in  $\text{VO}_2$  thin films. Figure from [81].

Even with good stoichiometry and appropriate crystal structure, the SMT characteristics are highly influenced by the  $\text{VO}_2$  microstructure. Figure 4.5 shows the modulation amplitude (left y-axis) and sharpness (right y-axis) of the SMT in  $\text{VO}_2$  thin films as a function of grain size [81]. The amplitude of the SMT (i.e. the modulation) increases with grain size: films with smaller grains have a higher density of grain boundaries and corresponding defects, resulting in a reduced electrical modulation across the SMT. Similarly, the sharpness of the transition increases with grain size: larger grains correspond to a lower grain boundary density, reducing electron scattering and making the transition more abrupt. Furthermore, the size distribution of grains also affects the transition sharpness: a

broad range of grain sizes causes a spread in  $T_C$  due to the dependence of oxygen non-stoichiometry on grain size, thus reducing the SMT sharpness [82].

Further, certain contradictory effects are seen with respect to grain size. Small grains in thin films are expected to broaden the hysteresis width [82]. Assuming uniform defect density for all grain sizes, smaller grains possess fewer nucleation defects capable of triggering the phase transition. Thus wider deviation from  $T_C$  in heating and cooling is required to exhibit the SMT, which leads to hysteresis widening [83]. This effect has been experimentally observed with smaller grains [84], but the opposite effect of hysteresis widening with larger grains has also been reported [85]. In this case, the widening is attributed to the longer annealing time required for larger grain growth, which can reduce the number of nucleation defects and thus cause broadening as above. This example highlights the competing effects that must be considered to understand the impact of morphology on thin film SMT characteristics.

There is reported potential for controlling the microstructure of  $\text{VO}_2$  thin films [84, 86], but the sensitivity of the fabrication processes limits the reproducibility. In a two-step fabrication process, as presented in this work, both the precursor film deposition and the post-deposition annealing process influence the resulting morphology. The conditions of the precursor film influence the microstructure of the resulting thin film, for example via stress influence of the substrate [87]. Similarly, the annealing temperature and oxidation pressure have a strong influence on the film grain structure [88]. These two processes also influence each other: for example, a higher density of grain boundaries in the precursor film increases the annealing oxidation rate due to oxygen diffusion through the grain boundaries, causing larger grain growth [66]. The vast number of competing effects indicates that  $\text{VO}_x$  thin film morphology requires careful optimisation for specific applications.

In addition to the SMT requirements, the desired characterisation and patterning approaches should also be considered. Certain applications may prioritise low levels of roughness and inhomogeneity, even over SMT amplitude or sharpness. For example, in this work,  $\text{VO}_2$  thin films are fabricated in order to perform post-deposition nanopatterning. SMT modulation is optimised by larger grains, but thin films with large grains are commonly rough and form 'open' layers, which are highly inappropriate for post-deposition patterning. Thus the fabrication of closed layers with some homogeneity is a priority in order to enable post-deposition fabrication of nanostructures.

## 4.2 Methods

### 4.2.1 Sample Fabrication

#### Substrate Preparation

Silicon (100) substrates of 12x12 mm were soaked in acetone to remove the wafer's protective resist layer, before being washed in isopropanol (IPA) and dried with an  $\text{N}_2$  gun prior to deposition.

Investigations into sample reproducibility led to substrate etching with hydrofluoric acid (HF) to remove the native  $\text{SiO}_2$  layer. The substrates were submerged in 1% HF for 1 minute, and then washed twice in deionized water to remove any HF residue. Subsequently, the substrates were soaked in IPA until the deposition step to ensure no oxidation of the Si. Just prior to deposition, the substrates were dried with an  $\text{N}_2$  gun and immediately placed into the deposition chamber.

#### Precursor Film Deposition: Electron-Beam Physical Vapour Deposition

Precursor thin films were deposited onto Si substrates via electron-beam physical vapour deposition (EB-PVD) in a Polyteknik Flextura M508E system. The deposition rate is controlled by the e-beam current and monitored by use of a quartz crystal monitor (QCM), which is calibrated by comparing to sample thickness measured by profilometry. In this case, the target crucible was vanadium, and the deposition rate was controlled to 0.05 nm/s. The e-beam current required to achieve this deposition rate ranged from 20 - 70 mA.

The main focus of this work is the optimisation of post-deposition annealing parameters, but the precursor material has significant influence on the annealing and oxidation process. Therefore investigations into two distinct precursor films were carried out:

1. *Pure (Non-Reactive) V Deposition*: The process takes place under high vacuum, depositing a thin film of pure vanadium.
2. *Reactive VO<sub>x</sub> Deposition*: O<sub>2</sub> gas at  $5 \times 10^{-3}$  mbar is entered into the vacuum chamber during the process in order to change the material composition of the deposited thin film from the target anode, V, to some oxidised layer VO<sub>x</sub>.

Multiple precursor thin films of both V and VO<sub>x</sub> were fabricated as detailed above. Parameters such as the deposition rate, O<sub>2</sub> flow pressure and substrate heating were varied to examine the effect on thin film stoichiometry and homogeneity. However, due to the challenges of optimising such a number of parameters, it was decided after initial tests that the substrate temperature would be kept at room temperature for both reactive and non-reactive precursor film deposition, to focus on post-deposition annealing parameters.

#### Post-Deposition Annealing: Hot Plate; Vacuum Furnace

Two annealing processes were examined in this work. The first, based on [74], consisted of isothermal, hot plate annealing of V thin films in air at ambient pressure. The hot plate was first ramped up to 480°C, found to be the optimal temperature for VO<sub>2</sub> formation, and precursor thin films were then annealed for a variable time (5 - 10 minutes) to investigate the optimum time for VO<sub>2</sub> formation. Immediately after being removed from the hot plate, the samples were cooled and stored in an N<sub>2</sub> desiccator to reduce any chance of oxidation.

The second method, based on [65], consisted of ramp annealing in a vacuum tube furnace with inlet O<sub>2</sub> gas. In this approach, both V and VO<sub>x</sub> thin films were used as precursors. The samples were loaded into a quartz tube in a loading chamber, which was pumped to  $10^{-5}$  mbar. The process chamber was pumped to high vacuum (base pressure  $10^{-6}$  mbar), and subsequently, O<sub>2</sub> gas was introduced from a 99.9% purity canister to a variable set point pressure of either  $10^{-4}$  mbar or  $10^{-3}$  mbar. Once the pressure was stabilised, the samples were entered into the process chamber and the furnace power was turned on. A maximum temperature of 500°C was chosen based on the results of Guo *et al.* [65], with a heating rate of approximately 40°C per minute. The annealing time was defined as the process time at this maximum temperature, and was varied from 15 - 240 minutes. After the desired annealing time, the furnace power was turned off, but the O<sub>2</sub> gas flow continued as the samples cooled inside the chamber. After cooling, the samples were stored in N<sub>2</sub> to limit potential oxidation in air.

### 4.2.2 Sample Characterisation

#### Rutherford Backscattering Spectrometry

Rutherford backscattering spectrometry (RBS) is an ion beam analysis technique to determine the elemental composition of thin films. To perform RBS, high energy He<sup>++</sup> nuclei are incident on a sample, elastically scattering as they interact with the material. The energy of the backscattered ions is detected as a function of scattering angle with respect to the incident beam, with specific energy channels corresponding to specific elements in the material (e.g. V and O). From the width of the spectral peaks at a given energy channel, the 'thin film units' (1 TFU =  $10^{15}$  atoms/cm<sup>2</sup>) of that element can be determined. Comparison of the different elemental peaks therefore gives the compositional ratio of the sample.

Channeling RBS measurements were performed on four VO<sub>x</sub> samples by Detect99 at Eindhoven University. Each was measured at two scattering angles (160°, 170°). The elemental ratio of O to V in each sample was determined by extracting TFU values from measured spectra. In addition, simulations were run to derive a measure of the samples' Gaussian thickness (i.e. an estimate for the thin film roughness). The measurements have a systematic error of 2% for all elements, all samples, and a statistical error of 3% for O and 1% for V.

### X-Ray Diffraction Analysis

The crystal structure of the samples was investigated using X-ray diffraction (XRD) analysis, measured with a Bruker D2 phaser. Two X-ray wavelengths,  $K\alpha_1 = 1.5406\text{\AA}$  and  $K\alpha_2 = 1.5406\text{\AA}$ , are generated by a Cu K $\alpha$  tube. These X-rays are incident on the sample at a variable angle  $\theta$ , and their interaction with the sample creates a diffraction pattern. At certain angles, constructive interference occurs following Bragg's Law:

$$n\lambda = 2d \sin \theta, \quad (4.1)$$

where  $n$  is the peak order,  $\lambda$  is the incident wavelength,  $d$  is the interplanar crystal lattice spacing, and  $\theta$  is the incident angle. As the incident angle is changed, the detector angle is similarly changed, such that the scattered X-ray intensity is measured normal to the incident ray. As the diffraction intensity depends on the lattice spacing, different crystal structures have characteristic peak positions. Comparison to reference data enables the determination of the sample crystallinity. In addition, XRD spectra can provide information about the grain size. According to the Scherrer equation [89]:

$$D = \frac{K\lambda}{\beta \cos \theta}, \quad (4.2)$$

where  $D$  is the average grain size,  $K$  is the Scherrer constant, and  $\beta$  is the XRD peak full-width-half-maximum (FWHM). Thus average grain size is inversely proportional to the FWHM of the XRD peak. This is explained by the increased number of crystallographic planes in larger grains, which cause stronger interference effects and subsequent sharpening of the XRD peaks.

## 4.3 Comparison of Demonstrative Samples

A wide range of parameters influence the fabrication of VO<sub>2</sub> thin films. In this section we discuss four demonstrative samples, fabricated with the aim of examining a spectrum of 'recipes', to highlight the dependence of thin film properties on deposition and annealing parameters. The four demo samples were fabricated as follows:

- **S1:** Reactive VO<sub>x</sub> Deposition & Oven Anneal at 500°C, 10<sup>-3</sup> mbar for 15 mins
- **S2:** Pure V Deposition & Oven Anneal at 500°C, 10<sup>-4</sup> mbar for 120 mins
- **S3:** Pure V Deposition & Oven Anneal at 500°C, 10<sup>-3</sup> mbar for 120 mins
- **S4:** Pure V Deposition & Ambient Anneal at 480°C for 7 mins

TABLE 4.1: RBS results for four demo samples, showing TFU values for O and V, resulting elemental ratio and deviation from the desired VO<sub>2</sub> value (O/V = 2), total TFU (a measure of thickness) and % variation (a measure of roughness).

Sample	O (TFU)	V (TFU)	O/V	% Deviation	Total (TFU)	% Variation
<b>S1</b>	773.9	397.7	<b>1.95</b>	-2.5%	1171.6	12.4%
<b>S2</b>	778.9	452.34	<b>1.72</b>	-14%	1231.24	13.4%
<b>S3</b>	813.3	464.95	<b>1.75</b>	-12.5%	1278.25	16.8%
<b>S4</b>	1087.2	470.61	<b>2.31</b>	+15.5%	1557.81	11.8%

### 4.3.1 Stoichiometry

Rutherford backscattering spectrometry was employed to determine the stoichiometry of the samples. Results are shown in Table 4.1, which presents the ‘thin film units’ (1 TFU =  $10^{15}$  atoms/cm<sup>2</sup>) of V and O, the subsequent O/V ratios, the % deviation from the desired O/V ratio of VO<sub>2</sub>, the TFU total, which is a measure of film thickness, and % variation, which is a measure of roughness for the films.

Stoichiometric VO<sub>2</sub> has an O/V ratio of 2. All samples show reasonable agreement with this value, with maximum variation of +15.5% seen for sample S4. The best stoichiometry is seen for S1, which has a ratio of 1.95, within 2.5% of the desired value and furthermore, within the error of 3% for O and 1% for V in addition to 2% systematic error. This is encouraging, highlighting reactive deposition followed by brief vacuum annealing as a promising fabrication method. The total thickness can be tentatively estimated by the TFU value, which suggests S1 is the thinnest sample.

Samples S2 and S3, on the other hand, with O/V ratios of 1.72 and 1.75, are under-oxidised. Both samples were fabricated via pure V deposition and long (120 mins) vacuum annealing, but the deviation of -14% and -12.5% from O/V = 2 shows that further annealing was required for oxidation to VO<sub>2</sub>. Comparison of these two samples shows a slight increase in oxidation level in S3 (annealed at  $10^{-3}$  mbar) than S2 (annealed at  $10^{-4}$  mbar). This seems appropriate considering that a higher oxygen pressure correlates to a higher oxidation rate, and thus an increased O/V ratio in a given time. It should be noted, however, that this difference is small (< 2%), within the margin of error. S3 appears to be slightly thicker than S2, again in agreement with a more oxidised film. However, the roughness of these samples is significantly different, with S3 possessing a thickness variation of 16.8% (the highest of all samples), and S2 a value of 13.4%. This highlights the annealing pressure as influential in determining morphology.

Finally, sample S4 has an O/V ratio of 2.31, suggesting that fabrication via pure V deposition followed by annealing in air results in an excess of oxygen. Due to the sensitivity of oxidation rates to oxygen partial pressure, it concurs that at high pressures, the time window for oxidation to VO<sub>2</sub> is very narrow. The over-oxidation in just 7 minutes compared to under-oxidised samples S1 (15 mins) and S2/S3 (120 mins) highlights the increased oxidation rate in ambient pressures. The total thickness of S4 is significantly higher than the other samples, but the thickness variation for S4 is not as high as that of S3, suggesting that over-oxidation is not necessarily related to increased roughness.



These results demonstrate that the oxidation levels of the four samples are consistent with the description of reaction kinetics presented in Section 4.1.1. At higher annealing pressures, the oxidation rate is increased, and ambient annealing is shown to have a very short critical time before over-oxidation. In addition, sample S1 shows highly desirable O/V stoichiometry, highlighting a promising fabrication approach. It is important to consider, however, that a significant limitation of RBS is the lack of distinction between layers in thin films. Considering the layered growth mechanism of  $\text{VO}_2$ , RBS is more valuable in combination with other characterisation methods, as presented below.

### 4.3.2 Crystallinity

In addition to correct stoichiometry, a monoclinic crystal structure is required to ensure the films will exhibit the appropriate SMT. X-ray diffraction (XRD) analysis can show whether  $\text{VO}_2(\text{M})$  formed in the demo samples. Figure 4.6 shows the four samples' XRD spectra, which are each normalised to their own highest intensity peak for ease of comparison. The annealing step is successful in crystallising all four samples, indicated by the sharp spectral peaks.

The spectrum of S4 demonstrates two characteristic peaks of  $\text{V}_2\text{O}_5$ , in agreement with the over-oxidation suggested by RBS. There is no suggestion of any  $\text{VO}_2$  within S4 from the XRD spectra. The sample is well-oriented to the (011) and (001) faces of  $\text{V}_2\text{O}_5$ , as demonstrated by the presence of peaks only at  $2\theta = 20^\circ, 21^\circ$  (according to JCPDS file No. 00-041-1426 [90]). The disparity between the expected  $\text{V}_2\text{O}_5$  stoichiometry (O/V = 2.5) and the measured ratio for S4 (O/V = 2.31) can be well explained by the  $\text{VO}_2$  growth model shown in Figure 4.4, in which a more oxygen-rich

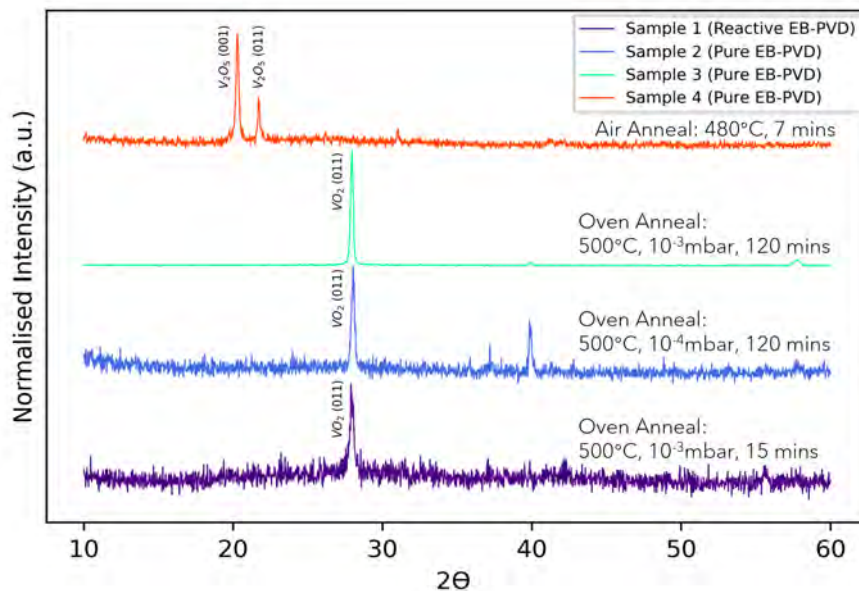


FIGURE 4.6: Normalised XRD spectra for samples S1, S2, S3, S4, displayed with a vertical offset for visibility. Each spectrum is normalised to its own highest intensity peak. Characteristic peaks are marked on the diagram, and fabrication parameters are indicated.

oxide layer forms on top of a more oxygen-deficient oxide layer. For the case of S4, this suggests a top layer of  $V_2O_5$  ( $O/V = 2.5$ ), with a less oxidised, mixed  $V_xO_y$  layer beneath ( $2 < O/V < 2.5$ ); thus the  $O/V$  ratio measured by RBS is smaller than 2.5 as it is rather an average of both layers. This highlights the importance of combining XRD and RBS results for sample interpretation.

Aside from S4, all three other samples exhibit a peak at  $2\theta = 28^\circ$ , corresponding to the (011) face of monoclinic  $VO_2$  (according to JCPDS file No. 01-076-0456 [90]). For S1, the spectrum is fairly noisy, showing only this (011) peak. This suggests that the sample displays strong preferential orientation of the (011)  $VO_2(M)$  face. The RBS and XRD results are again in agreement with the  $VO_2$  growth model: RBS results for S1,  $O/V = 1.95$ , are within 3% of that expected for  $VO_2$ . This indicates that the majority of the film could be stoichiometric  $VO_2$ ; the small reduction to the overall stoichiometry could be explained by some under-oxidised grains within the film. The XRD signal noise and lack of any other characteristic peaks suggests these grains are composed of mixed phases ( $V_xO_y$ ) that do not display crystallinity, or are randomly orientated such that no other crystal planes show significant interference. These results suggest this sample is predominantly  $VO_2(M)$ .

S2 similarly displays the  $28^\circ$  peak for  $VO_2(M)$ , with slightly lower signal noise than S1. The improved signal to noise ratio (SNR) suggests better oriented grains and/or the presence of fewer alternate crystals in S2 than S1. There are additional peaks at  $37^\circ$  and  $40^\circ$  which could correspond to  $VO_2(M)$ . However, this is not certain as there are a number of other vanadium oxide crystals that exhibit XRD peaks around these values. To confirm the origin of these additional peaks, further measurements should be taken. Regardless, the strong peak at  $28^\circ$  indicates that this sample contains a significant amount of monoclinic  $VO_2$ .

The XRD spectrum for S3 displays the same  $28^\circ$  peak of  $VO_2(M)$ , with a very sharp and low-noise signal. A small peak at approximately  $58^\circ$  corresponds to the second order diffraction of the (011) face, and the small peak seen in S2 at  $40^\circ$  is again seen in S3. The sharp peaks and high SNR suggest very strong diffraction from the  $VO_2(M)$  (011) crystal face. This indicates that the sample is highly oriented, with minimal contributions from other crystal structures. However, considering the sample is found to be under-oxidised by RBS ( $O/V = 1.75$ ), the total thin film composition cannot be solely  $VO_2$ . This low oxygen stoichiometry again indicates the presence of less oxidised material within the film. Unlike S1 and S2, however, the lack of signal noise in S3 suggests minimal presence of other (non- $VO_2(M)$ ) grains, in contrast with the measured stoichiometry.

To understand why S3 exhibits an under-oxidised stoichiometry alongside such a high intensity XRD signal from monoclinic  $VO_2$ , we consider the Scherrer formula (Equation 4.2), which states that the full-width-half-maximum (FWHM) of the XRD peak is inversely proportional to the average grain size. Figure 4.7 shows the XRD spectra centred on the  $VO_2(M)$  (011) peaks for S1, S2 and S3, which shows a narrower FWHM for S3 than for S1 and S2. This indicates that S3 has larger

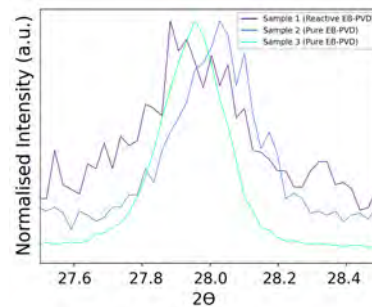


FIGURE 4.7: XRD spectra for S1, S2, and S3, zoomed into the (011)  $VO_2(M)$  peak.

grains, which might explain the highly preferential orientation required to exhibit such a low-noise XRD signal. In films with smaller grains, a more random grain distribution occurs due to grains growing on top of each other rather than directly on the substrate. On the other hand, samples with larger grains exhibit less random orientation, and if the grains are large enough that the thin film is a single grain layer, preferential growth is increased due to the influence of the substrate. Thus thin films with larger grains are likely to exhibit high SNRs and sharp XRD peaks due to this enhanced orientation. Scanning electron microscopy (SEM) is now presented to examine if this is the case for these samples, and to probe the morphologies further.

### 4.3.3 Morphology

Finally, the samples were examined via SEM imaging to investigate the microstructure and examine the fabrication parameters influential in determining the morphology. SEM images were taken in a FEI Verios 460 or a Thermo Fisher Quanta 650, at 10 kV acceleration voltage and 100 pA current. Figure 4.9 shows SEM images from the four samples discussed above. Note that the magnification is not consistent.

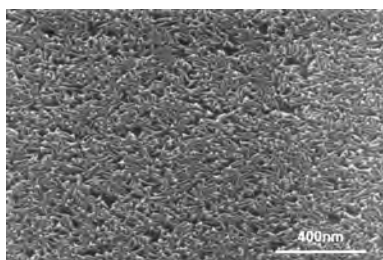


FIGURE 4.8: SEM image of pure V thin film before annealing treatment.

As with the XRD and RBS results, S4 is immediately distinct from the other samples: where S1, S2 and S3 are all made up of grains (Figures 4.9(a-c)), the surface of S4 is composed of flakes, with clumped material mounds scattered across the surface (Figure 4.9(d)). To understand this texture, it is helpful to consider the precursor film of pure V used for samples S2, S3, and S4. Figure 4.8 shows the flakey morphology of a vanadium thin film deposited by EB-PVD, prior to post-deposition annealing. The high-pressure (ambient) and fast (7 mins) annealing of S4 ap-

pears to have oxidised parts the film into clumps, while other parts have remained in a similar state to this precursor film. In S2 and S3, on the other hand, the low annealing pressures ( $10^{-4} - 10^{-3}$  mbar) reduce the oxidation rate, enabling the gradual formation of grains with no evidence of the flakey precursor microstructure.

Samples S1 and S2 have similar film structures and comparable grain sizes ( $< 100$  nm). There are a number of ‘pinholes’ in both films that appear to go right through to the substrate. S3, on the other hand, is made up of larger grains ( $\approx 200 - 400$  nm), and also larger holes ( $> 100$  nm) which expose significant parts of the substrate. Due to the larger grains, the roughness in S3 is likely significantly higher than S1 or S2. Although S1 and S2 are not perfectly-closed thin film layers, the grains appear to be fairly well-packed, whereas S3 forms an open layer, with spaces between grains.

These findings are consistent with the XRD results discussed above. S3 showed a narrow peak width and significantly higher SNR than S1 and S2, and it was suggested that this was due to larger grains and subsequent highly oriented growth. As seen in Figure 4.9(c), the large grains in S3 form a single grain layer, such that the substrate has a strong effect on the preferred orientation. Alternatively, the smaller grains in S1 and S2 (Figures 4.9(a,b)) appear to grow on top of each other, and are small enough to fill in holes in the film. This explains the lower SNR of the XRD



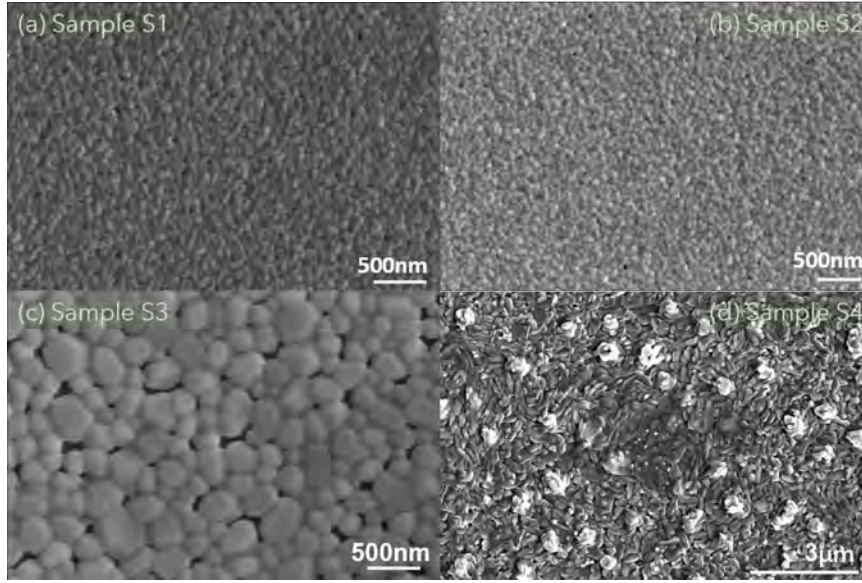


FIGURE 4.9: SEM images of (a) S1 (b) S2 (c) S3 (d) S4.

spectra for S1 and S2, and is also in good agreement with the peak width comparisons above.

It is not clear, however, how exactly these findings relate to the fabrication parameters. S1 was made from reactive deposition, whereas S2 and S3 were based on pure V deposition. All three were annealed in the tube oven, S1 at  $10^{-3}$  mbar for 15 mins; S2 at  $10^{-4}$  mbar for 120 mins; S3 at  $10^{-3}$  mbar for 120 mins. There are a number of changing parameters in these samples, but there appears to be an interplay between reactive deposition (where the precursor film has some oxygen content before annealing), the annealing pressure, and the annealing time. For example, S1 (reactive  $\text{VO}_x$  deposition) and S3 (pure V deposition) were annealed at the same pressure ( $10^{-3}$  mbar) but for 15 mins and 120 mins respectively. Thus the small grains of S1 and large grains of S3 could be explained in a number of ways, such as longer annealing times leading to larger grain growth (as seen in [76]), or the presence of oxygen in the precursor film encouraging the growth of smaller grains.

A further comparison of S2 and S3 is interesting, because although they possess similar RBS ratios and XRD spectra, the grain growth is highly affected by the annealing pressure. Both samples were fabricated identically, other than different annealing pressures. From these SEM comparisons, it appears that the higher annealing pressure of S3 is responsible for larger grain growth. This could be explained by the reduced oxidation rate at lower pressures, which could exhibit slow crystallisation.

Considering that the aim of this work is to produce thin film samples for the fabrication of nanostructures, the optimal thin film morphology must be appropriate for post-deposition patterning, as well as strong SMT modulation. As detailed in Section 4.1.2, thin films with smaller grains, such as S1 and S2, show suppression of SMT amplitude due to a high density of grain boundaries. The larger grains in S3 should minimise this suppression, but the large gaps in the film could still affect the SMT characteristics due to the inhomogeneity and roughness of the layer. Furthermore, for the fabrication of nanocylinders of  $d \approx 200$  nm, S3 is entirely inappropriate due to the grain size being comparable to the size of the desired nanostructures.

### 4.3.4 Summary

Of the four demo recipes, only S4 (*pure V deposition; air anneal at 480°C for 7 mins*) is not appropriate for VO<sub>2</sub> thin film fabrication, due to strong evidence of over-oxidation to the higher valence V<sub>2</sub>O<sub>5</sub>. The other three are promising starter recipes for stoichiometric, crystalline VO<sub>2</sub> thin film fabrication. The RBS elemental ratio of S1 (*reactive VO<sub>x</sub> deposition; oven anneal at 500°C, 10<sup>-3</sup> mbar for 15 mins*) was the closest to the desired value, suggesting very good stoichiometry (O/V = 1.95). The very high SNR and sharp monoclinic VO<sub>2</sub> XRD peak of S3 (*pure V deposition; oven anneal at 500°C, 10<sup>-3</sup> mbar for 120 mins*), however, indicates highly preferential grain orientation and good monoclinic crystallinity. Furthermore, the morphologies of S2 (*pure V deposition; oven anneal at 500°C, 10<sup>-4</sup> mbar for 120 mins*) and S1 were far more appropriate for post-fabrication patterning than S3 due to the smaller, tightly packed grains; the corresponding increase in grain boundary density, however, is likely to suppress the switching amplitude of optical properties at the SMT, which could restrict the modulation depth measured during PP-CL.

## 4.4 Additional Findings

The results discussed in Section 4.3 are in good agreement with the literature presented in Section 4.1, highlighting the vast number of process parameters and their complex impact on the resulting thin films. A study into the influence of substrate preparation, deposition type, and annealing pressure and time was undertaken to further optimise the recipe for closed-layer, crystalline, stoichiometric VO<sub>2</sub> thin films. In particular, we investigate how these parameters could be tuned to enhance the formation of well-oriented VO<sub>2</sub>(M) crystallites, enable control of the grain size and homogeneity, and ensure fabrication recipes that are reproducible.

- **Annealing in air is found to consistently over-oxidise samples:** based on the excess oxidation levels of S4, air annealing was investigated further to verify if VO<sub>2</sub> films could be formed by changing the annealing time. Figure 4.10(a) shows XRD spectra from S4 with three additional samples fabricated similarly (*pure V deposition followed by air anneal at 480°C*), but with varying annealing times of 3, 5 and 30 mins. All samples exhibit the XRD peaks characteristic of V<sub>2</sub>O<sub>5</sub>, so ambient annealing was deemed inappropriate for the purposes of VO<sub>2</sub> fabrication. Note that the SNR of these spectra increases with higher annealing times, indicating higher levels of crystallinity and orientation.
- **Reactive deposition produces amorphous thin films:** even with substrate heating up to 300°C during deposition, reactive VO<sub>x</sub> films are amorphous prior to annealing, but show strong crystallinity after annealing. Figure 4.10(b) shows the XRD spectra for two sample films, G1 and G2, fabricated by reactive VO<sub>x</sub> deposition prior to and after oven annealing at 500°C, 10<sup>-3</sup> mbar, for 120 and 30 mins respectively. Both samples display an extremely broad signal before annealing due to their amorphous state, but after oxidation, the spectra both show a strong peak for VO<sub>2</sub>(M) (011) and a high SNR, indicating that the annealing step is successful in crystallising the films.

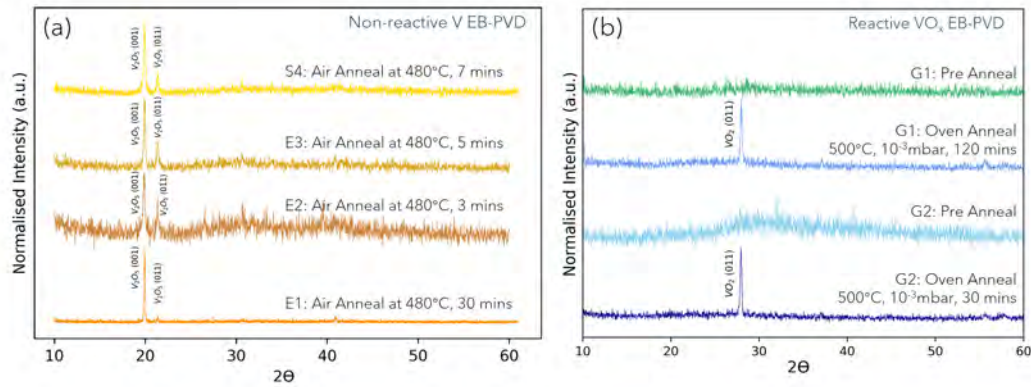


FIGURE 4.10: (a) XRD spectra of four samples made via pure V deposition, followed by annealing in air at 480°C for 30 mins (E1), 3 mins (E2), 5 mins (E3) and 7 mins (S4). (b) Comparison of XRD spectra of two samples fabricated by reactive  $\text{VO}_x$  deposition before and after post-deposition oven annealing at 500°C,  $10^{-3}$  mbar, for 30 mins (G2) and 120 mins (G1). Note that the spectra are each normalised to their own highest peak, and displayed with a vertical offset for viewing purposes.

- **Annealing pressure and time have significant influence on grain size:** Figure 4.11 shows SEM images of V films deposited by non-reactive EB-PVD and subsequently annealed in the tube oven at  $10^{-3}$  or  $10^{-4}$  mbar, for 60 or 120 mins. The morphology comparison demonstrates that higher annealing pressures and longer annealing times lead to the formation of larger grains. It also appears that as grain growth increases, larger holes are formed in the thin films. Thus if small grains are preferred (for example, to allow post-deposition patterning), low pressures and shorter process times are beneficial.

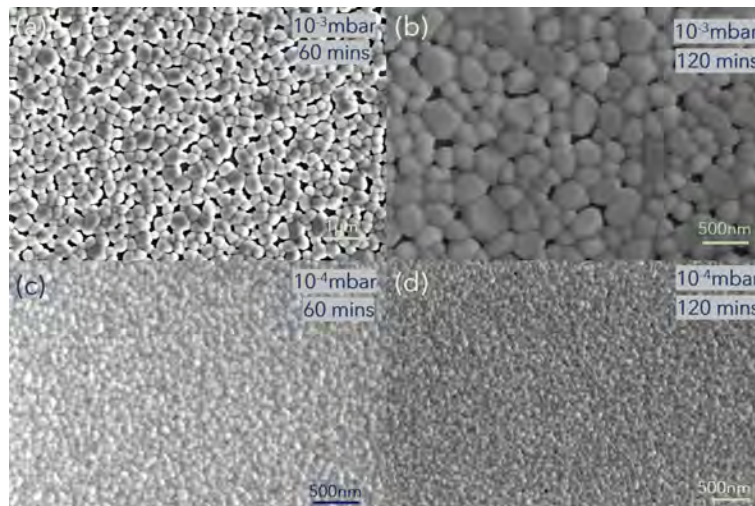


FIGURE 4.11: SEM comparison of pure V thin films after annealing in the tube oven at (a)  $10^{-3}$  mbar for 60 mins (b)  $10^{-3}$  mbar for 120 mins (c)  $10^{-4}$  mbar for 60 mins (d)  $10^{-4}$  mbar for 120 mins.

- **Reproducibility of fabrication is improved at higher annealing pressures:** Figure 4.12 shows XRD spectra for identical pure V films annealed at 500°C for 60 mins at either (a)  $10^{-4}$  mbar, or (b)  $10^{-3}$  mbar. There appears to be a lack of reproducibility of XRD spectra for samples annealed at  $10^{-4}$  mbar, demonstrated by the additional peaks and range of SNRs between samples in Figure 4.12(a). As the samples annealed at  $10^{-3}$  mbar show improved consistency in their XRD spectra, it is likely that the tube oven chamber is unstable at such low pressures. This highlights the sensitivity of fabrication to experimental variation.

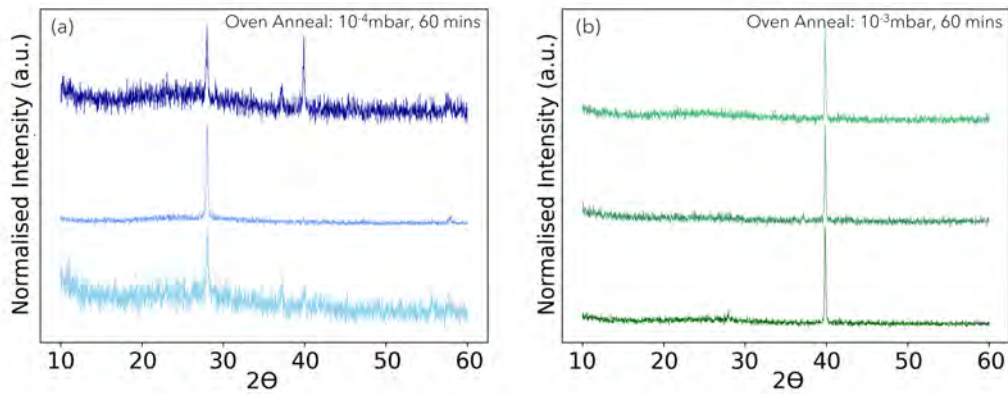


FIGURE 4.12: XRD spectra for two sets of three identical samples, fabricated by pure V EB-PVD and post-deposition oven annealing. Annealing conditions: 500°C, 60 mins, at (a)  $10^{-4}$  mbar (b)  $10^{-3}$  mbar. Note that the spectra are each normalised to their own highest peak, and displayed with a vertical offset for viewing purposes.

- **Substrate preparation to remove native oxide ( $\text{SiO}_2$ ) has significant impact on grain formation:** Figure 4.13 shows a comparison of how substrate preparation impacts thin film  $\text{VO}_2$  growth. A single Si substrate was prepared with hydrofluoric acid (HF) to remove the native  $\text{SiO}_2$  layer. Afterwards, one half of the substrate was soaked in IPA, while the other half was left in contact with air for 5 days to allow thermal oxide growth. Then a pure V film was deposited via non-reactive EB-PVD, followed by tube oven annealing at  $10^{-3}$  mbar for 60 mins. The SEM comparisons demonstrate the drastic difference in microstructure from the part of the sample treated with acetone (Figure 4.13(a)) which exhibits large grains and many holes through to the substrate, to the part treated with HF (Figure 4.13(b)), which shows small, tightly packed grains in a completely closed layer. The morphological differences are likely due to different lattice matching between the substrates (with or without the native layer of  $\text{SiO}_2$ ) and  $\text{VO}_2$ . Thus, to minimise the growth of open layer films with large grains and holes, HF substrate preparation is promising.



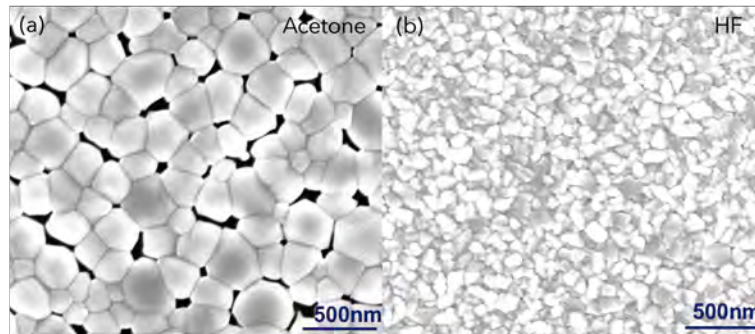


FIGURE 4.13: SEM images for comparison of a single-sample of  $\text{VO}_2$  in which half the substrate was prepared with (a) acetone, and the other half with (b) HF.

## 4.5 Conclusions and Outlook

Although the optical switching capabilities of our fabricated films are yet to be demonstrated, these investigations into stoichiometry, crystallinity, and morphology present a range of successful fabrication recipes for  $\text{VO}_2$  thin films. We have demonstrated the strong influence of fabrication parameters on the resulting sample qualities, and draw attention to the most important considerations for thin film optimisation, including the balance between SMT suppression and thin film microstructure.

This work shows that a two-step process for  $\text{VO}_2$  thin film fabrication has the potential to produce highly stoichiometric, crystalline (monoclinic) samples, with a range of morphologies that can be tuned via annealing pressure and time. Reactive  $\text{VO}_x$  deposition followed by oven annealing is shown to result in extremely good stoichiometry ( $\text{O}/\text{V} = 1.95$ ), and high levels of monoclinic crystallinity and preferential orientation. In addition, these samples show small, tightly packed grains, making them suitable for patterning purposes, but likely causing suppression of SMT modulation. On the other hand, pure V deposition followed by oven annealing demonstrates reasonable stoichiometries ( $\text{O}/\text{V} = 1.72, 1.75$ ), and strong evidence of monoclinic  $\text{VO}_2$  crystallinity. However, the grain growth in these samples is far more controllable; by reducing annealing pressure or time, or by removing the substrate native oxide, the grain size can be significantly reduced. Future work could examine the findings in this thesis systematically to thoroughly investigate the influence of these parameters, with the potential to further optimise  $\text{VO}_2$  thin film fabrication for specific applications and desired characteristics.

For the continuation of this thesis, samples fabricated by reactive  $\text{VO}_x$  EB-PVD and subsequent oven annealing are chosen. This is based on the balance of good stoichiometry, strong monoclinic crystallinity, and tightly packed grain structure appropriate for patterning. In the following chapter, we fabricate and characterise  $\text{VO}_2$  nanocylinders based on this thin film recipe.

## Chapter 5

# Nanocylinder Fabrication and Characterisation

*Following the geometric and thin film optimisation processes examined in the previous chapters, here we present preliminary patterning and characterisation results of VO<sub>2</sub> nanostructures for optical resonance switching in the visible. Post-deposition focused ion beam milling is investigated as a simple method to pattern thin film VO<sub>2</sub>. We show cathodoluminescence (CL) measurements of varying geometries to examine the geometrical resonances excited within these VO<sub>2</sub> nanostructures. These CL spectra are compared to finite-difference-time-domain simulations in order to further examine the suitability of the sample design and fabrication methods presented in this thesis. Finally, suggestions are made for changes to the milling process to improve the isotropy and geometry of the nanostructures, and considerations for CL signal enhancement are discussed.*

### 5.1 Focused Ion Beam Milling

A number of VO<sub>2</sub> thin films fabricated via reactive electron beam physical vapour deposition (EB-PVD) and subsequent oven annealing (see Section 4 for further details) were investigated for post-deposition patterning via focused ion beam milling (FIB). This method was chosen over etching due to a lack of established etch processes and the volatility of VO<sub>2</sub>'s etch mechanism [91], and because of the simple single nanocylinder design.

Structures were milled in a FEI Helios Nanolab 600 Scanning Electron Microscope (SEM) combined with a FIB Sidewinder Gallium Liquid Metal Ion Source (Ga LMIS), using an ion beam current of 28 pA, an acceleration voltage of 30 kV, and a donut geometry design of 300 nm inner diameter and 2  $\mu$ m outer diameter. FIB milling of polycrystalline samples such as these VO<sub>2</sub> films can be challenging due to ion channelling, which causes uneven sputtering rates across a sample depending on grain structure and orientation [92]. This effect has a significant impact on the required beam dosage, motivating testing to determine appropriate experimental settings. In this section, three structures fabricated during the dosage testing are examined.

Figure 5.1 shows three structures patterned by FIB milling into thin film VO<sub>2</sub> of approximately 200 nm height. The dosage rates for each structure were varied by changing the number of ion beam scans (number of passes), while all other experimental parameters were fixed as detailed above. Structure A was milled with 1500 passes, structure B with 2200 passes, and structure C with 2800 passes. As anticipated, different dosage rates produce distinct geometries with several artifacts: structure A shows milling into the VO<sub>2</sub> thin film, with some small holes exposing

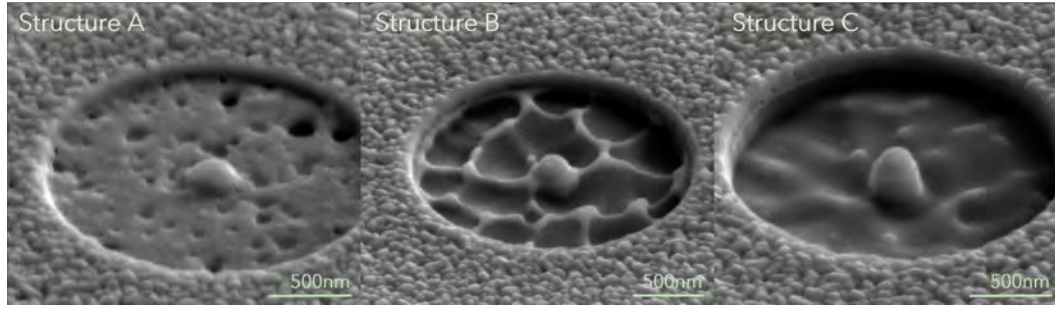


FIGURE 5.1: SEM images showing the three FIB milled structures.

the Si substrate, and a slightly rounded cylinder of  $\text{VO}_2$ ; structure B exhibits more extensive albeit uneven ablation, exposing more of the Si substrate but leaving behind ridges of  $\text{VO}_2$  and a rounded  $\text{VO}_2$  nanocylinder, which sits on top of a small Si pillar; finally, structure C shows milling through the entire  $\text{VO}_2$  layer, exposing the Si substrate and showing a rounded  $\text{VO}_2$  nanocylinder on top of a larger Si pillar.

The first apparent artifact is the rounding of the  $\text{VO}_2$  cylinders in all three structures. This occurs due to the Gaussian shape of the ion beam [92]. At low dosages, this effect is minimal, but as the dosage increases, the higher exposure of the material to this Gaussian ion beam causes more significant rounding, which can also reduce the structure diameter. This effect is evidenced by the flatter, wider shape of the  $\text{VO}_2$  in structure A, and more rounded, narrow shape in structure C.

Avoiding high beam dosages should prevent such significant rounding of the  $\text{VO}_2$  structures. Lower dosages, however, are not sufficient to ensure milling through the entire layer of  $\text{VO}_2$ . This is further complicated by the uneven milling demonstrated in all three structures, caused by thin film polycrystallinity and random grain orientation. This effect is consistent with the sample characterisation in Section 4.3, where XRD spectra demonstrated that the thin films were polycrystalline and exhibited a range of grain orientations. The use of polycrystalline Si substrates further enhances this effect, as seen in structure B in particular.

At lower beam dosages, undesired areas of  $\text{VO}_2$  are left unmilled, such as in structures A and B. This could complicate investigations of phase switching dynamics as the structure would not be isolated from the rest of the thin film. Increasing the dosage, however, leads to milling of the Si substrate and the formation of Si pillars beneath the  $\text{VO}_2$  structures. This effect is seen in structures B and C. These Si pillars are of the order of a few hundred nm in diameter, and thus under photon or electron excitation would host Mie-like resonances in the visible spectral range [93]. The optical response of these structures and the possible interaction between the  $\text{VO}_2$  and Si resonators is investigated via cathodoluminescence measurements in Section 5.2.

## 5.2 Cathodoluminescence Measurements

Cathodoluminescence (CL) measurements were performed using a Thermo Fisher Quanta 650 SEM equipped with a Schottky field emission gun (FEG). The emission of cathodoluminescence after electron excitation of a sample was collected by a parabolic mirror, and directed into a spectrometer. CL measurements presented in this work were taken at 10 keV electron energies.

These measurements were performed on the three structures shown in Figure 5.1 to investigate the resonant response of the different geometries. Secondary electrons were measured in addition to the CL spectra, to enable the correlation of spectral features with the spatial map of the structures. Figures 5.2(a-c) show unnormalised CL spectra at different positions of these structures (green and blue lines) alongside the spatially integrated CL spectra from the unpatterned VO<sub>2</sub> thin film (grey line). The SEM inset has green and blue markers showing the positions on each structure that correspond to the shown CL spectra. Two-dimensional CL intensity maps are shown in Figures 5.2(d-i), demonstrating the modal light confinement at the resonance wavelengths indicated by the CL spectra.

The CL spectra for the three structures (green and blue lines) in Figures 5.2(a-c) demonstrate clear peaks, indicating the excitement of optical resonances within the structures. To verify that these are geometric resonances, the CL spectrum from the unpatterned VO<sub>2</sub> thin film (grey line) is shown in the same plots. The broad, flat spectrum shows no evidence of excited resonances before thin film patterning. Thus it is evident that nanopatterning of the VO<sub>2</sub> films is responsible for the excitation of resonances.

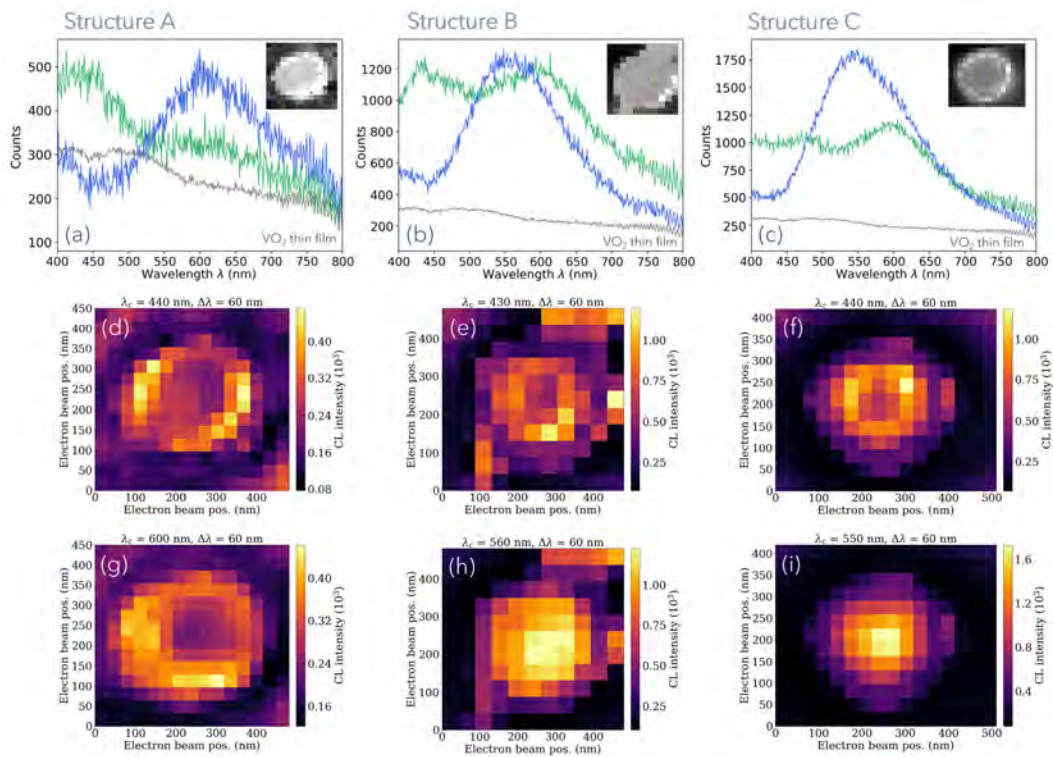


FIGURE 5.2: (a-c) Cathodoluminescence (CL) spectra at two different positions on each structure. The inset shows the secondary electron map collected simultaneously alongside the CL signal, with the blue and green markers corresponding to the spectra shown. The grey spectra is the spatially integrated CL signal from the unpatterned VO<sub>2</sub> thin film. Figures correspond to: (a) structure A (b) structure B (c) structure C. (d-i) Two-dimensional CL intensity maps at the resonance wavelengths indicated in (a-c). Note that these spectra were not corrected for the variable collection efficiency.



In structure A, the CL spectra show peaks at approximately  $\lambda = 440$  nm (green line) and  $\lambda = 600$  nm (blue line), suggesting resonant excitation at these wavelengths. The CL maps corresponding to these wavelengths are shown in Figures 5.2(d) and (g) respectively. The CL maps of both resonances display a donut shape, with higher intensity at the edges of the structure, resembling electric quadrupole (EQ)-like modes [93]. However, it is difficult to assign these resonances to specific modes, especially as we would expect a low-order mode profile at  $\lambda = 600$  nm. Regardless, the intensity maps and CL spectra suggest geometrical resonances have been excited.

Structures B and C display similar evidence of optical resonances. The CL spectra for structure B show peaks at approximately  $\lambda = 440$  nm and  $\lambda = 600$  nm (green line), and  $\lambda = 560$  nm (blue line). The CL intensity maps corresponding to  $\lambda = 440$  nm and  $\lambda = 560$  nm are shown in Figures 5.2(e) and (h) respectively. The lower wavelength resonance ( $\lambda = 440$  nm) exhibits a faint, ring-shaped intensity map, which appears EQ-like, suggesting it could be a higher order mode [93]. At the higher wavelength resonance ( $\lambda = 560$  nm), the intensity instead peaks at the centre of the structure, with minimal CL response at the structure edges. This appears electric dipole (ED)-like, and could be the lower order mode.

Structure C exhibits a strong CL peak at  $\lambda = 550$  nm (blue line), focused at the centre of the structure (see SEM inset). In addition (green line), a broad, merged peak appears around  $\lambda = 400$  nm - 480 nm, and another peak is seen at  $\lambda = 600$  nm. Note that the broad peak around 440 nm could be impacted by the reduced collection efficiency response of the measurement. Similarly to structure B, the CL intensity map is ring-shaped at the lower wavelength resonance ( $\lambda = 440$  nm, Figure 5.2(f)), which could again correspond to a higher order, EQ-like mode. At the higher wavelength resonance ( $\lambda = 550$  nm, Figure 5.2(i)), the intensity map instead peaks at the centre of the structure. This suggests excitation of the lowest order, ED-like mode [93].

The CL maps shown in Figure 5.2 for structures B and C appear to show low-order, ED-like modes at  $\lambda = 560$  nm and  $\lambda = 550$  nm respectively, and higher-order, EQ-like modes at  $\lambda = 430$  nm and  $\lambda = 440$  nm respectively. The CL spectra demonstrate that when exciting the centre of the cylinders with the electron beam (blue pixels in SEM inset / blue lines), the higher-order resonance is not excited in either structure. This is explained by the presence of a node at the cylinder centre, which makes it more difficult to couple to the higher-order mode. Furthermore, at the edges of the cylinders (green pixels in SEM inset / green lines), structures B and C both display two spectral peaks, suggesting successful excitation of a low- and high- order mode. This is in agreement with the higher-order mode being easier to couple to at a position away from the central cylinder node.

From comparison of the spectra from the centre (blue) and edge (green) of the cylinders, it appears that when the electron beam excites near the edge of the cylinders, the low-order mode shifts from  $\lambda = 560$  nm for structure B and  $\lambda = 550$  nm for structure C, to  $\lambda = 600$  nm for both structures. As detailed above, the CL maps at  $\lambda = 560$  nm and  $\lambda = 550$  nm (Figures 5.2(h) and (i)) appear to be low-order, ED-like modes. The CL maps corresponding to  $\lambda = 600$  nm for both structures are shown in Appendix A, confirming that these also appear to be low-order, ED-like modes. Thus the position of the electron beam on the nanostructures seems to change the resonance wavelengths of the low-order modes, with a red-shift occurring when the electron beam excites the centre rather than the edge of the structures. It is not clear what causes this shift, but it could be related to the non-ideal shape of the structures.

As the resonances excited within these structures are expected to be geometrical resonances, the geometry of the nanostructures should strongly influence the CL response. The CL intensity maps for structure A show significant asymmetry, which is likely due to the asymmetry of the structure itself. There is some reduced asymmetry seen in structure B, and in structure C, the CL intensity maps seem fairly symmetric. Furthermore, the collected CL signal is very low for structure A, but this increases significantly for structure B, and once again for structure C. Thus it seems that the introduction of Si pillars beneath the  $\text{VO}_2$  structure improves the symmetry and enhances the signal of the response, further evidence that these are geometric resonances.

As detailed in Section 3.2, the optimisation of the sample design for PP-CL requires a balance between maximising the modulation of the resonance switching and ensuring a high enough CL signal for collection. The low signal exhibited by structure A could pose complications for PP-CL measurements, whereby we use a pulsed electron beam which further reduces the CL signal. The introduction of a Si pillar beneath the  $\text{VO}_2$  cylinder appears to enhance the CL response, suggesting structures B and C might be more appropriate for PP-CL. We now consider whether a combined Si -  $\text{VO}_2$  nanostructure could exhibit sufficient modulation.

### 5.2.1 Comparison to Simulation

The preliminary CL measurements presented in Section 5.2 suggest that structure C, made up of a Si cylinder beneath the  $\text{VO}_2$  structure, exhibits the strongest CL response, and is thus of interest for PP-CL. To examine this possibility further, we reran finite-difference-time-domain (FDTD) simulations (setup details are in Section 3.2.1), using a half-sphere and cylinder shape to mimic the geometries of structures A and C. Figure 5.3 shows the simulated scattering cross-sections for both the low-

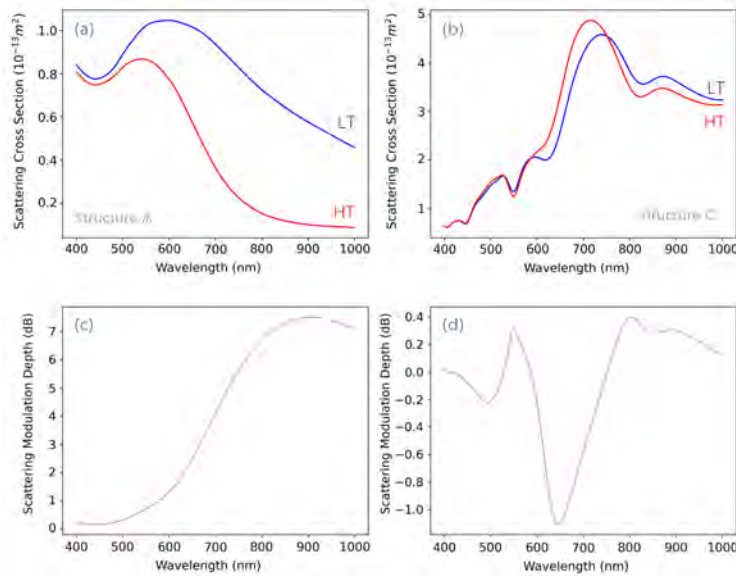


FIGURE 5.3: **(a-b)** Simulated scattering cross-sections for the low-temperature phase (LT) and high-temperature phase (HT) of **(a)** structure A, **(b)** structure C. **(c-d)** Corresponding scattering modulation depth for **(c)** structure A **(d)** structure C.

and high- temperature phases and the extracted scattering modulation depth for structures A and C.

Figures 5.3(a-b) demonstrate that the scattering intensities of structure C are significantly higher than structure A. This confirms that the introduction of the Si pillar increases the scattering response, in some agreement with the CL spectra comparisons above. In addition, the VO<sub>2</sub> – Si structure exhibits a far more complex scattering response than the VO<sub>2</sub> cylinder alone, displaying a number of additional peaks which could correspond to the higher order modes excited within Si nanostructures of approximately this size [93]. The higher index of Si than VO<sub>2</sub> leads to better mode confinement, increasing the scattering response. Furthermore, the high losses in VO<sub>2</sub> are known to suppress the exhibition of magnetic modes [18], whereas the lower losses in Si enable electric and magnetic mode excitation, which could explain the higher order peaks seen in Figure 5.3(b) that are not displayed in Figure 5.3(a).

The CL spectra peaks for structures A and C, as shown in Figures 5.2(a) and (c), do not show much agreement with the simulated resonances in Figures 5.3(a) and (b). The FDTD simulations measure all-directional scattering under plane wave illumination, which does not closely model CL excitation [93]. Furthermore, the optical properties of VO<sub>2</sub> are taken from literature ellipsometry data [18]. Due to the highly sensitive fabrication process and its resulting effect on material properties, these values are not consistent for all thin films of VO<sub>2</sub> [4]. Thus the refractive index data used in simulation is likely different to that of the fabricated nanostructures, limiting the comparison between experiment and simulation.

Qualitatively, however, these simulations are significant. The low- and high- temperature scattering cross-sections for structure C appear very similar in shape, indicating that the switching of VO<sub>2</sub> does not significantly influence the scattering spectra. This suggests that the Si cylinder dominates both the hot and cold spectra. Figure 5.3(d) demonstrates this explicitly, with the maximum modulation depth for structure C reaching (-)1 dB. Structure A, on the other hand, exhibits a maximum modulation depth of 7 dB, shown in Figure 5.3(c). This is a drastic improvement, and confirms that the inclusion of an Si pillar in these structures dominates over the phase switching. Thus although structure C demonstrates a strong CL signal, the reduced modulation depth shows that a hybrid Si - VO<sub>2</sub> structure would not be appropriate for phase transition investigations such as the proposed PP-CL.

### 5.3 Improved Milling Approach

The fabrication of VO<sub>2</sub> structures can be improved via the use of a protective etch mask. As shown in Figure 5.1, the FIB milled VO<sub>2</sub> structures are rounded and their size is reduced due to high exposure to the Gaussian ion beam. The use of a mask layer on top of a sample could mitigate these issues by reducing rounding, enabling the fabrication of more cylinder-like geometries. As the shape and size of a nanocylinder influence the resonant scattering strength and spectral confinement, the ability to more carefully design and fabricate cylindrical structures could enable enhancement of the scattering signal.

Figure 5.4 shows a structure milled into a VO<sub>2</sub> thin film with a photoresist layer and chromium (Cr) coating. The thin film was prepared by cleaning in acetone and rinsing in IPA, before baking for 1 minute at 150°C to remove any water content. Then, S1805 resist was dropped onto the sample as it was rotated in a Suss Delta 80

spin-coater. The sample was then baked for a further minute to develop the 200 nm resist layer, before a 30 nm layer of Cr was deposited onto the sample using the Leica EM ACE600 Double Sputter Coater. The sample was then patterned as above in the Helios FIB-SEM. After patterning, the samples can be soaked in acetone to remove the resist and Cr layer, to leave behind a flat-topped structure.

The use of this protective mask layer appears to be promising to reduce rounding of the structures as seen in Figure 5.1. This approach, however, was not successful in mitigating the problem of milling into the substrate. A range of FIB parameters were investigated, but as seen in Figure 5.4, although the structure shape is more cylindrical (but some sloping of the sidewalls), there is still inconsistent milling into the substrate.

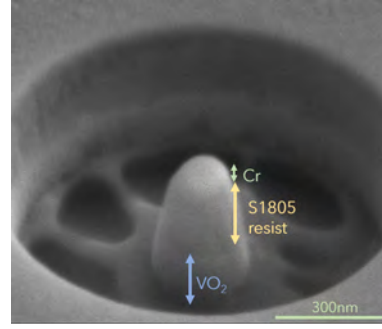


FIGURE 5.4: SEM image showing a FIB milled structure into a  $\text{VO}_2$  thin film with a 200 nm S1805 resist layer and a 30 nm Cr layer to act as a hard etch mask.

## 5.4 Conclusions and Outlook

In this section we have presented preliminary fabrication and characterisation of three  $\text{VO}_2$  nanostructures. FIB milling is shown to be an appropriate approach for post-deposition patterning of the thin films optimised in Section 4, and CL measurements demonstrate that the fabricated nanostructures exhibit geometrical resonances. The single-layer  $\text{VO}_2$  structure exhibits a low CL signal, which is enhanced in the  $\text{VO}_2$  - Si structures. However, qualitative comparison of FDTD simulations and the measured CL demonstrates that in these hybrid  $\text{VO}_2$  - Si structures, the resonance switching modulation is suppressed by the dominance of the Si. Thus we suggest optimisation of the  $\text{VO}_2$  structure shape is the most promising approach to enhance the CL signal for phase transition characterisation via PP-CL.

The use of a resist and Cr mask during FIB milling is shown to minimise the rounding of the structures, with the potential to increase the scattering response. Extensive optimisation of this approach is outside the scope of this work, but further studies to investigate the effect of the resist on the sensitive material parameters of  $\text{VO}_2$  are recommended, and extensive dosage testing should be carried out to further minimise side-wall sloping and substrate etching. Furthermore, dual optimisation of the thin film fabrication and FIB milling could couple the processes, enabling significant improvements to this nanofabrication, for example through tuning the grain size via annealing pressure or time.

The FDTD simulations presented in this work have measured all-directional scattering under plane-wave excitation. These could be improved via the use of dipole point sources to more closely model the response of structures to CL excitation [93]. In addition, the use of optical properties from literature rather than measured data from the fabricated  $\text{VO}_2$  complicates the comparison between simulation and experiment. Future work would benefit greatly from the use of a temperature-dependent ellipsometry setup, whereby thin film optical properties could be measured and used in subsequent simulations to ensure the modelled  $n, k$  values match those in experiment.

## Chapter 6

# Conclusions & Outlook

In this thesis we have demonstrated an extensive optimisation process for the design and fabrication of optically resonant  $\text{VO}_2$  nanostructures. Pump-probe cathodoluminescence spectroscopy (PP-CL) is presented as a novel measurement technique to examine the semiconductor-metal-transition (SMT) of  $\text{VO}_2$  with high resolution in space and time. We use finite-difference-time-domain (FDTD) simulations to show that a single-nanocylinder-on-substrate is appropriate for PP-CL characterisation, and then exploit the geometric tunability of the resonant response to optimise the design. A two-step fabrication procedure based on low-temperature electron-beam physical vapour deposition and high-temperature annealing is optimised to produce highly stoichiometric ( $\text{O}/\text{V} = 1.95$ ) and crystalline (monoclinic,  $\text{VO}_2(\text{M})$ )  $\text{VO}_2$  thin films. Furthermore, an investigation into the morphology of a range of samples demonstrates the tunability of grain size and microstructure by controlling annealing pressure and time. We then demonstrate the nanopatterning of an optimised  $\text{VO}_2$  thin film via focused ion beam (FIB) milling, and present preliminary cathodoluminescence (CL) measurements that show the excitement of optical resonances within these structures. Through comparison to FDTD simulations, we discuss opportunities for CL signal enhancement via geometric optimisation and present an improved approach for FIB milling of  $\text{VO}_2$  thin films.

## 6.1 Outlook

This work has demonstrated the wide potential of a simple  $\text{VO}_2$  nanocylinder-on-substrate sample, which presents the dual opportunity to probe underlying material properties while investigating novel nanophotonic functionality. We suggest that the design and fabrication approaches presented in this thesis could be used as a guideline for  $\text{VO}_2$  sample fabrication for examination of SMT modulation and dynamics via PP-CL or other characterisation techniques.

Moreover, the careful examination of geometric and material parameters has highlighted a number of avenues for future work, such as control over grain growth during annealing and the influence of substrate preparation on thin film properties. Further investigation based on these results could enable a number of interesting sample designs. For example, if grains are grown large enough to exhibit geometrical resonances, the grains themselves could be used as  $\text{VO}_2$  resonators for phase switching measurements, removing the need for post-deposition patterning. Furthermore, the presented fabrication process for  $\text{VO}_2$  thin films could be used for the fabrication of hybrid systems, whereby single resonators or nanostructure arrays could be made from another material, and a  $\text{VO}_2$  thin film above or below these structures could modulate the resonant response as it changes phase.



Most significantly, the exhibition of geometric resonances within the VO<sub>2</sub> nanostructures proves the successful fabrication of a sample to display optical resonance switching for PP-CL. Thus we believe the next step is to use the samples from this work to bring this novel and unique characterisation of VO<sub>2</sub> into reality.

## *Acknowledgements*

After more than a year working on this project, I have lots of people to acknowledge and thank for their support and guidance. First, I want to say a massive thank you to Albert, for giving me the opportunity to join the group, and for all your wisdom and enthusiasm. The way that you lead your group results in such a friendly and inviting environment, and I feel very grateful to have been a part of it. And indeed, I'm already looking forward to returning in a few months time! I also want to say thank you to Jorik van de Groep for being the second examiner of this work and taking the time to read my thesis.

An enormous thank you also goes to Nika! I have learnt a huge amount from you over the last year, and I am so grateful for your supervision. I had many (!) questions, and even when the topics were somewhat new to you as well, you always took the time to delve into them with me. Your help with the writing and editing process was invaluable: thank you for showing me how to say more with fewer words. You also taught me a lot about persisting, even when it seems like everything that could go wrong, does go wrong. And thanks for being a lovely officemate and always having a smile on your face!

I also have to say thanks to all the other members of the Polman group for the laughs over the last year. Andrea, Evelijn, Hannah, Magda, Matthias, Nika, Robin, Saskia, Stefan, Tom: thank you for making the group so welcoming and always being keen to help. I don't think there is a single one of you who has not sat down with me at some point to share your wisdom, and it has been very inspiring to work alongside you all. And a special thank you to Matthias and Evelijn for training me and sharing their CL knowledge.

Within AMOLF, I must also thank the cleanroom staff for many trainings and many questions. In particular, thank you to Igor for taking the time to help me understand what was happening to the vanadium when I had no clue. Even when nothing seemed to make sense, our discussions were very helpful!

Finally, I need to thank my lovely friends and family, who have listened to me complain about vanadium dioxide for way more hours than they deserve. Elaina, thanks for always cheering me up with tea and biscuits and for letting me stay with you when I had nowhere to go. Jasmin, thank you for your calm wisdom and for listening to, and providing me with, endless hours of voicenotes. Hallie, thank you for all the funny chats and always helping to put things into perspective.

Thank you to Stian, for having the patience of a saint and trying your absolute best to follow along when I talk physics. And Cristina, thank you for always listening to my stories from the lab and laughing along with(/at) me. Thanks to all the other pals in Amsterdam for a brilliant two years. And to my friends in the UK who patiently wait months at a time for whatsapp replies, but still act as if I never left once I make it back home.

Last but not least, thank you to dad for the technical support and mum for the emotional support, and both of you for always guiding me and also for being so much fun! I miss you and the sisters massively, and I am very grateful for everything you do for me.

## Appendix A

# Additional Cathodoluminescence Intensity Maps

Figure A.1 shows the CL intensity maps for structures B and C at the (higher wavelength) resonance peaks indicated by the CL spectra in Figure 5.2. It is apparent from the CL maps shown here that at both  $\lambda = 560$  nm and  $\lambda = 600$  nm for structure B, and both  $\lambda = 550$  nm and  $\lambda = 600$  nm for structure C, the excited modes appear to be low-order, and ED-like. As discussed in Section 5.2, the spectral position of these low-order modes appears to shift to higher wavelengths when the electron beam is exciting the edge of the cylinder rather than the centre of the cylinder. It is not clear why this wavelength shift occurs, but the maps show that the spatial modes within the structures do not change significantly.

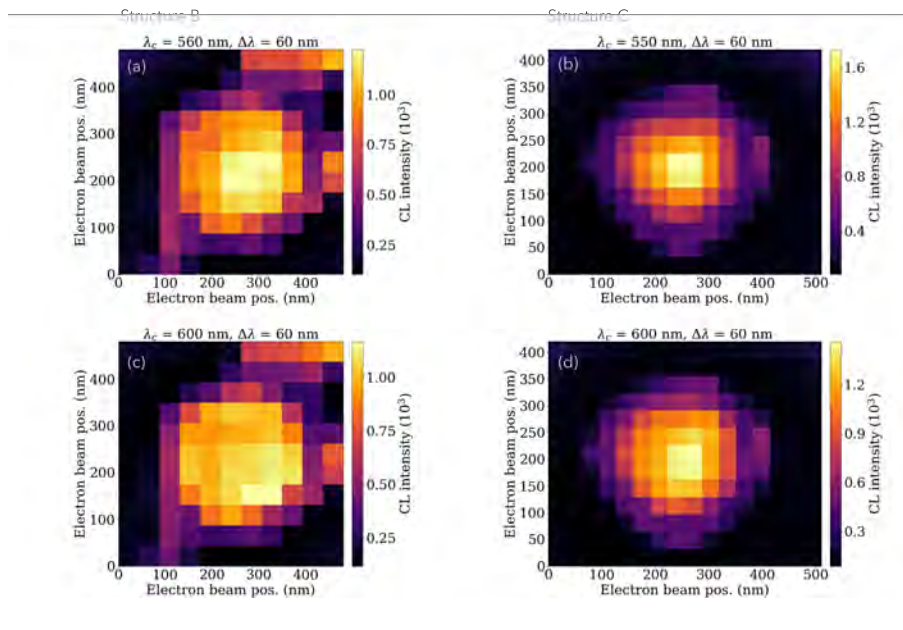


FIGURE A.1: Two-dimensional CL intensity maps for structure B: (a)  $\lambda = 560$  nm and (c)  $\lambda = 600$  nm, structure C: (b)  $\lambda = 550$  nm and (d)  $\lambda = 600$  nm.

# Bibliography

- [1] Simone Raoux et al. *Phase change materials - mrs bulletin*. 2012. URL: <https://link.springer.com/article/10.1557/mrs.2011.357>.
- [2] Nazmul Habib, Chung Hon Lam, and Robert McMahon. *Phase change material based temperature sensor*.
- [3] Matthias Wuttig. "Non-volatile photonic applications with phase-change materials". In: *Photonic and Phononic Properties of Engineered Nanostructures XI* (2021). DOI: [10.1117/12.2589497](https://doi.org/10.1117/12.2589497).
- [4] Sébastien Cueff et al. "Vo2nanophotonics". In: *APL Photonics* 5.11 (2020), p. 110901. DOI: [10.1063/5.0028093](https://doi.org/10.1063/5.0028093).
- [5] F. J. Morin. "Oxides which show a metal-to-insulator transition at the neel temperature". In: *Physical Review Letters* 3.1 (1959), 34–36. DOI: [10.1103/physrevlett.3.34](https://doi.org/10.1103/physrevlett.3.34).
- [6] Elizabeth E. Chain. "Optical properties of vanadium dioxide and vanadium pentoxide thin films". In: *Applied Optics* 30.19 (1991), p. 2782. DOI: [10.1364/ao.30.002782](https://doi.org/10.1364/ao.30.002782).
- [7] Yujie Ke et al. "Vanadium dioxide: The multistimuli responsive material and its applications". In: *Small* 14.39 (2018), p. 1802025. DOI: [10.1002/smll.201802025](https://doi.org/10.1002/smll.201802025).
- [8] M. Soltani et al. "Optical switching of vanadium dioxide thin films deposited by reactive pulsed laser deposition". In: *Journal of Vacuum Science and Technology A: Vacuum, Surfaces, and Films* 22.3 (2004), p. 859. DOI: [10.1116/1.1722506](https://doi.org/10.1116/1.1722506).
- [9] Matthias Wuttig and Noboru Yamada. "Phase-change materials for rewritable data storage". In: *Nature Materials* 6.11 (2007), 824–832. DOI: [10.1038/nmat2009](https://doi.org/10.1038/nmat2009).
- [10] Sergey V. Makarov et al. "Light-induced tuning and reconfiguration of nanophotonic structures". In: *Laser and Photonics Reviews* 11.5 (2017), p. 1700108. DOI: [10.1002/lpor.201700108](https://doi.org/10.1002/lpor.201700108).
- [11] T. Driscoll et al. "Dynamic tuning of an infrared hybrid-metamaterial resonance using vanadium dioxide". In: *Applied Physics Letters* 93.2 (2008), p. 024101. DOI: [10.1063/1.2956675](https://doi.org/10.1063/1.2956675).
- [12] Matthew J. Dicken et al. "Frequency tunable near-infrared metamaterials based on VO<sub>2</sub> phase transition". In: *Optics Express* 17.20 (2009), p. 18330. DOI: [10.1364/oe.17.018330](https://doi.org/10.1364/oe.17.018330).
- [13] Zheng Yang and Shriram Ramanathan. "Breakthroughs in photonics 2014: Phase change materials for Photonics". In: *IEEE Photonics Journal* 7.3 (2015), 1–5. DOI: [10.1109/jphot.2015.2413594](https://doi.org/10.1109/jphot.2015.2413594).
- [14] Mikhail A. Kats et al. "Ultra-thin perfect absorber employing a tunable phase change material". In: *Applied Physics Letters* 101.22 (2012), p. 221101. DOI: [10.1063/1.4767646](https://doi.org/10.1063/1.4767646).
- [15] Jura Rensberg et al. "Active optical metasurfaces based on defect-engineered phase-transition materials". In: *Nano Letters* 16.2 (2016), 1050–1055. DOI: [10.1021/acs.nanolett.5b04122](https://doi.org/10.1021/acs.nanolett.5b04122).

- [16] Nikita A. Butakov et al. "Switchable plasmonic–dielectric resonators with metal–insulator transitions". In: *ACS Photonics* 5.2 (2017), 371–377. DOI: [10.1021/acsp Photonics.7b00334](https://doi.org/10.1021/acsp Photonics.7b00334).
- [17] Yonghui Kim et al. "Phase modulation with electrically tunable vanadium dioxide phase-change metasurfaces". In: *Nano Letters* 19.6 (2019), 3961–3968. DOI: [10.1021/acs.nanolett.9b01246](https://doi.org/10.1021/acs.nanolett.9b01246).
- [18] Peter Kepić et al. "Optically tunable mie resonance vo2 nanoantennas for meta-surfaces in the visible". In: *ACS Photonics* 8.4 (2021), 1048–1057. DOI: [10.1021/acsp Photonics.1c00222](https://doi.org/10.1021/acsp Photonics.1c00222).
- [19] Arseniy I. Kuznetsov et al. "Optically resonant dielectric nanostructures". In: *Science* 354.6314 (2016). DOI: [10.1126/science.aag2472](https://doi.org/10.1126/science.aag2472).
- [20] Yanqing Zhang et al. "Recent Progress on Vanadium Dioxide Nanostructures and Devices: Fabrication, Properties, Applications and Perspectives". In: *Nano-materials* 11.2 (2021), p. 338. DOI: [10.3390/nano11020338](https://doi.org/10.3390/nano11020338).
- [21] Joyeeta Nag and R F Haglund Jr. "Synthesis of vanadium dioxide thin films and nanoparticles". In: *Journal of Physics: Condensed Matter* 20.26 (2008), p. 264016. DOI: [10.1088/0953-8984/20/26/264016](https://doi.org/10.1088/0953-8984/20/26/264016).
- [22] Zewei Shao et al. "Recent progress in the phase-transition mechanism and modulation of vanadium dioxide materials". In: *NPG Asia Materials* 10.7 (2018), 581–605. DOI: [10.1038/s41427-018-0061-2](https://doi.org/10.1038/s41427-018-0061-2).
- [23] Magdalena Solà-Garcia et al. *Pump-probe cathodoluminescence microscopy*. 2021. DOI: [10.48550/ARXIV.2112.03034](https://doi.org/10.48550/ARXIV.2112.03034). URL: <https://arxiv.org/abs/2112.03034>.
- [24] John B. Goodenough. "The two components of the crystallographic transition in VO<sub>2</sub>". In: *Journal of Solid State Chemistry* 3.4 (1971), 490–500. DOI: [10.1016/0022-4596\(71\)90091-0](https://doi.org/10.1016/0022-4596(71)90091-0).
- [25] Guillermo Guzman et al. "Electrical switching in VO<sub>2</sub>sol–gel films". In: *J. Mater. Chem.* 6.3 (1996), 505–506. DOI: [10.1039/jm9960600505](https://doi.org/10.1039/jm9960600505).
- [26] Yuanjie Xu et al. "Synthesis and properties of MO and W ions co-doped porous nano-structured VO<sub>2</sub> films by Sol–Gel Process". In: *Journal of Sol-Gel Science and Technology* 64.2 (2012), 493–499. DOI: [10.1007/s10971-012-2881-9](https://doi.org/10.1007/s10971-012-2881-9).
- [27] W. Brückner, U. Gerlach, and B. Thuss. "Phase diagram of V<sub>1-x</sub>Al<sub>x</sub>O<sub>2</sub>". In: *Physica Status Solidi (a)* 40.2 (1977). DOI: [10.1002/pssa.2210400248](https://doi.org/10.1002/pssa.2210400248).
- [28] M. Marezio et al. "Structural aspects of the metal-insulator transitions in CR-doped V". In: *Physical Review B* 5.7 (1972), 2541–2551. DOI: [10.1103/physrevb.5.2541](https://doi.org/10.1103/physrevb.5.2541).
- [29] Sung-Hwan Bae et al. "The memristive properties of a single vo2nanowire with switching controlled by self-heating". In: *Advanced Materials* 25.36 (2013), 5098–5103. DOI: [10.1002/adma.201302511](https://doi.org/10.1002/adma.201302511).
- [30] Shamashis Sengupta et al. "Field-effect modulation of conductance in VO<sub>2</sub> nanobeam transistors with HFO<sub>2</sub> as the gate dielectric". In: *Applied Physics Letters* 99.6 (2011), p. 062114. DOI: [10.1063/1.3624896](https://doi.org/10.1063/1.3624896).
- [31] Michael F. Becker et al. "Femtosecond laser excitation of the semiconductor-metal phase transition in vo<sub>2</sub>". In: *Applied Physics Letters* 65.12 (1994), 1507–1509. DOI: [10.1063/1.112974](https://doi.org/10.1063/1.112974).
- [32] Daesu Lee et al. "Sharpened vo<sub>2</sub> phase transition via controlled release of epitaxial strain". In: *Nano Letters* 17.9 (2017), 5614–5619. DOI: [10.1021/acs.nanolett.7b02482](https://doi.org/10.1021/acs.nanolett.7b02482).
- [33] Hyojin Yoon et al. "Reversible phase modulation and hydrogen storage in multivalent VO<sub>2</sub> epitaxial thin films". In: *Nature Materials* 15.10 (2016), 1113–1119. DOI: [10.1038/nmat4692](https://doi.org/10.1038/nmat4692).



- [34] Zheng Yang, Changhyun Ko, and Shriram Ramanathan. "Oxide Electronics utilizing ultrafast metal-insulator transitions". In: *Annual Review of Materials Research* 41.1 (2011), 337–367. DOI: [10.1146/annurev-matsci-062910-100347](https://doi.org/10.1146/annurev-matsci-062910-100347).
- [35] Run Shi et al. "Recent advances in fabrication strategies, phase transition modulation, and advanced applications of vanadium dioxide". In: *Applied Physics Reviews* 6.1 (2019), p. 011312. DOI: [10.1063/1.5087864](https://doi.org/10.1063/1.5087864).
- [36] Hyun-Tak Kim et al. "Monoclinic and correlated metal phase in VO<sub>2</sub> as evidence of the Mott Transition: Coherent Phonon Analysis". In: *Physical Review Letters* 97.26 (2006). DOI: [10.1103/physrevlett.97.266401](https://doi.org/10.1103/physrevlett.97.266401).
- [37] G.J. Hyland. "Semiconductor Metal Phase transitions". In: *Journal of Solid State Chemistry* 2.3 (1970), 318–331. DOI: [10.1016/0022-4596\(70\)90090-3](https://doi.org/10.1016/0022-4596(70)90090-3).
- [38] N F Mott. "The basis of the electron theory of metals, with special reference to the transition metals". In: *Proceedings of the Physical Society. Section A* 62.7 (1949), 416–422. DOI: [10.1088/0370-1298/62/7/303](https://doi.org/10.1088/0370-1298/62/7/303).
- [39] "The mott transition and the hubbard model". In: *Quantum Electron Liquids and High-T<sub>c</sub> Superconductivity* (1995), 151–173. DOI: [10.1007/978-3-540-47678-8\\_7](https://doi.org/10.1007/978-3-540-47678-8_7).
- [40] Daniel Wegkamp and Julia Stähler. "Ultrafast Dynamics during the photoinduced phase transition in VO<sub>2</sub>". In: *Progress in Surface Science* 90.4 (2015), 464–502. DOI: [10.1016/j.progsurf.2015.10.001](https://doi.org/10.1016/j.progsurf.2015.10.001).
- [41] G.A Toombs. "Quasi-one-dimensional conductors". In: *Physics Reports* 40.3 (1978), 181–240. DOI: [10.1016/0370-1573\(78\)90149-7](https://doi.org/10.1016/0370-1573(78)90149-7).
- [42] F. Grandi, A. Amaricci, and M. Fabrizio. "Unraveling the mott-peierls intrigue in vanadium dioxide". In: *Physical Review Research* 2.1 (2020). DOI: [10.1103/physrevresearch.2.013298](https://doi.org/10.1103/physrevresearch.2.013298).
- [43] Cédric Weber et al. "Vanadium Dioxide: A Peierls-Mott Insulator Stable against Disorder". In: *Physical Review Letters* 108.25 (2012). DOI: [10.1103/physrevlett.108.256402](https://doi.org/10.1103/physrevlett.108.256402). URL: <https://doi.org/10.1103/%2Fphysrevlett.108.256402>.
- [44] J. Laverock et al. "Direct observation of decoupled structural and electronic transitions and an ambient pressure monocliniclike metallic phase of VO<sub>2</sub>". In: *Physical Review Letters* 113.21 (2014). DOI: [10.1103/physrevlett.113.216402](https://doi.org/10.1103/physrevlett.113.216402).
- [45] Vance R. Morrison et al. "A photoinduced metal-like phase of monoclinic vo<sub>2</sub> revealed by Ultrafast Electron Diffraction". In: *Science* 346.6208 (2014), 445–448. DOI: [10.1126/science.1253779](https://doi.org/10.1126/science.1253779).
- [46] Manuel Decker and Isabelle Staude. "Resonant dielectric nanostructures: A low-loss platform for functional nanophotonics". In: *Journal of Optics* 18.10 (2016), p. 103001. DOI: [10.1088/2040-8978/18/10/103001](https://doi.org/10.1088/2040-8978/18/10/103001).
- [47] Craig F. Bohren and Donald R. Huffman. "Absorption and scattering of light by small particles". In: (1998). DOI: [10.1002/9783527618156](https://doi.org/10.1002/9783527618156).
- [48] Jorik van de Groep. "Resonant nanophotonic structures for photovoltaics". PhD thesis. University of Amsterdam, 2015.
- [49] Stefan A. Maier. *Plasmonics*. Springer, 2007.
- [50] Gustav Mie. "Beiträge zur Optik trüber medien, Speziell Kolloidaler metal-lösungen". In: *Annalen der Physik* 330.3 (1908), 377–445. DOI: [10.1002/andp.19083300302](https://doi.org/10.1002/andp.19083300302).
- [51] J. van de Groep and A. Polman. "Designing dielectric resonators on substrates: Combining magnetic and electric resonances". In: *Optics Express* 21.22 (2013), p. 26285. DOI: [10.1364/oe.21.026285](https://doi.org/10.1364/oe.21.026285).
- [52] Lijun Jiang and William N. Carr. "Vanadium Dioxide Thin Films for Thermo-Optical Switching Applications". In: *MRS Proceedings* 785 (2003). DOI: [10.1557/proc-785-d10.4](https://doi.org/10.1557/proc-785-d10.4).

- [53] Kai Liu et al. "Recent progresses on physics and applications of vanadium dioxide". In: *Materials Today* 21.8 (2018), 875–896. DOI: [10.1016/j.mattod.2018.03.029](https://doi.org/10.1016/j.mattod.2018.03.029).
- [54] A. Cavalleri et al. "Femtosecond structural dynamics in VO<sub>2</sub> during an ultrafast solid-solid phase transition". In: *Physical Review Letters* 87.23 (2001). DOI: [10.1103/physrevlett.87.237401](https://doi.org/10.1103/physrevlett.87.237401).
- [55] Renske M. van der Veen et al. "Single-nanoparticle phase transitions visualized by four-dimensional electron microscopy". In: *Nature Chemistry* 5.5 (2013), 395–402. DOI: [10.1038/nchem.1622](https://doi.org/10.1038/nchem.1622).
- [56] Thomas Danz, Till Domröse, and Claus Ropers. "Ultrafast nanoimaging of the order parameter in a structural phase transition". In: *Science* 371.6527 (2021), 371–374. DOI: [10.1126/science.abd2774](https://doi.org/10.1126/science.abd2774).
- [57] Lukas Novotny and Bert Hecht. "Principles of nano-optics". In: (2012). DOI: [10.1017/cbo9780511794193](https://doi.org/10.1017/cbo9780511794193).
- [58] Joris Schefold et al. "Spatial resolution of Coherent Cathodoluminescence Super-Resolution Microscopy". In: *ACS Photonics* 6.4 (2019), 1067–1072. DOI: [10.1021/acsp Photonics.9b00164](https://doi.org/10.1021/acsp Photonics.9b00164).
- [59] Magda Sola Garcia. "Electron-matter interaction probed with time-resolved cathodoluminescence". PhD thesis. University of Amsterdam, 2021.
- [60] MPPC modules C14455 series. URL: [https://www.hamamatsu.com/content/dam/hamamatsu-photonics/sites/documents/99\\_SALES\\_LIBRARY/ssd/c14455-1550ga\\_etc\\_kacc1283e.pdf](https://www.hamamatsu.com/content/dam/hamamatsu-photonics/sites/documents/99_SALES_LIBRARY/ssd/c14455-1550ga_etc_kacc1283e.pdf).
- [61] *High-performance photonic simulation software*. 2022. URL: <https://www.lumerical.com/>.
- [62] Edward D. Palik. *Handbook of Optical Constants of Solids*. Academic Press, 1985.
- [63] Marie Anne van de Haar et al. "Controlling magnetic and electric dipole modes in hollow silicon nanocylinders". In: *Optics Express* 24.3 (2016), p. 2047. DOI: [10.1364/oe.24.002047](https://doi.org/10.1364/oe.24.002047).
- [64] László Pósa et al. "A Rational Fabrication Method for Low Switching-Temperature VO<sub>2</sub>". In: *Nanomaterials* 11.1 (2021), p. 212. DOI: [10.3390/nano11010212](https://doi.org/10.3390/nano11010212).
- [65] Pengfei Guo et al. "Vanadium dioxide phase change thin films produced by thermal oxidation of metallic vanadium". In: *Thin Solid Films* 707 (2020), p. 138117. DOI: [10.1016/j.tsf.2020.138117](https://doi.org/10.1016/j.tsf.2020.138117).
- [66] Geert Rampelberg. "Thin Film Synthesis of VO<sub>2</sub> and VN by Gas-Solid Reactions and Atomic Layer Deposition". PhD thesis. Ghent University, 2016.
- [67] A. L. Pergament et al. "On the Problem of Metal-Insulator Transitions in Vanadium Oxides". In: *ISRN Condensed Matter Physics* 2013 (2013), pp. 1–6. DOI: [10.1155/2013/960627](https://doi.org/10.1155/2013/960627).
- [68] Youn-Bae Kang. "Critical evaluation and thermodynamic optimization of the VO–VO<sub>2.5</sub> system". In: *Journal of the European Ceramic Society* 32.12 (2012), pp. 3187–3198. DOI: [10.1016/j.jeurceramsoc.2012.04.045](https://doi.org/10.1016/j.jeurceramsoc.2012.04.045).
- [69] A. Mukherjee and S.P. Wach. "An investigation of the kinetics and stability of VO<sub>2</sub>". In: *Journal of the Less Common Metals* 132.1 (1987), pp. 107–113. DOI: [10.1016/0022-5088\(87\)90178-0](https://doi.org/10.1016/0022-5088(87)90178-0).
- [70] Miloslav Pekař. "Thermodynamic Driving Forces and Chemical Reaction Fluxes; Reflections on the Steady State". In: *Molecules* 25.3 (2020), p. 699. DOI: [10.3390/molecules25030699](https://doi.org/10.3390/molecules25030699).
- [71] Koen M. Martens et al. "VO<sub>2</sub>, a Metal-Insulator Transition Material for Nanoelectronic Applications". In: *ECS Transactions* 45.4 (2012), pp. 151–158. DOI: [10.1149/1.3700465](https://doi.org/10.1149/1.3700465).

- [72] B. E. Deal and A. S. Grove. "General Relationship for the Thermal Oxidation of Silicon". In: *Journal of Applied Physics* 36.12 (1965), pp. 3770–3778. DOI: [10.1063/1.1713945](https://doi.org/10.1063/1.1713945).
- [73] Haixin Zhang. "Uniformity of VO<sub>2</sub> phase change material (PCM) thin films produced by thermal oxidation of vanadium". PhD thesis. University of Dayton, 2021.
- [74] Geert Rampelberg et al. "In situ X-ray diffraction study of the controlled oxidation and reduction in the V–O system for the synthesis of VO<sub>2</sub> and V<sub>2</sub>O<sub>3</sub> thin films". In: *Journal of Materials Chemistry C* 3.43 (2015), pp. 11357–11365. DOI: [10.1039/c5tc02553b](https://doi.org/10.1039/c5tc02553b).
- [75] C. H. Griffiths and H. K. Eastwood. "Influence of stoichiometry on the metal-semiconductor transition in vanadium dioxide". In: *Journal of Applied Physics* 45.5 (1974), pp. 2201–2206. DOI: [10.1063/1.1663568](https://doi.org/10.1063/1.1663568).
- [76] V. A. Klimov et al. "Effect of crystallization of amorphous vanadium dioxide films on the parameters of a semiconductor-metal phase transition". In: *Semiconductors* 37.4 (2003), pp. 370–374. DOI: [10.1134/1.1568452](https://doi.org/10.1134/1.1568452).
- [77] Yuzo Shigesato, Mikiko Enomoto, and Hidehumi Odaka. "Thermochromic VO<sub>2</sub> Films Deposited by RF Magnetron Sputtering Using V<sub>2</sub>O<sub>3</sub> or V<sub>2</sub>O<sub>5</sub> Targets". In: *Japanese Journal of Applied Physics* 39.Part 1, No. 10 (2000), pp. 6016–6024. DOI: [10.1143/jjap.39.6016](https://doi.org/10.1143/jjap.39.6016).
- [78] J. Leroy et al. "Structural, electrical and optical properties of thermochromic VO<sub>2</sub> thin films obtained by reactive electron beam evaporation". In: *Thin Solid Films* 520.14 (2012), pp. 4823–4825. DOI: [10.1016/j.tsf.2011.08.035](https://doi.org/10.1016/j.tsf.2011.08.035).
- [79] Srinivasa Rao Popuri et al. "Rapid Hydrothermal Synthesis of VO<sub>2</sub> (B) and Its Conversion to Thermochromic VO<sub>2</sub> (M1)". In: *Inorganic Chemistry* 52.9 (2013), pp. 4780–4785. DOI: [10.1021/ic301201k](https://doi.org/10.1021/ic301201k).
- [80] J.-C. Valmalette and J.-R. Gavarri. "High efficiency thermochromic VO<sub>2</sub>(R) resulting from the irreversible transformation of VO<sub>2</sub>(B)". In: *Materials Science and Engineering: B* 54.3 (1998), pp. 168–173. DOI: [10.1016/S0921-5107\(98\)00148-2](https://doi.org/10.1016/S0921-5107(98)00148-2).
- [81] D. Brassard et al. "Grain size effect on the semiconductor-metal phase transition characteristics of magnetron-sputtered VO<sub>2</sub> thin films". In: *Applied Physics Letters* 87.5 (2005), p. 051910. DOI: [10.1063/1.2001139](https://doi.org/10.1063/1.2001139).
- [82] V. A. Klimov et al. "Hysteresis loop construction for the metal-semiconductor phase transition in vanadium dioxide films". In: *Technical Physics* 47.9 (2002), pp. 1134–1139. DOI: [10.1134/1.1508078](https://doi.org/10.1134/1.1508078).
- [83] Eugenii Donev. "Metal-semiconductor transitions in nanoscale vanadium dioxide - thin films, subwavelength holes, and nanoparticles". PhD thesis. Vanderbilt University, 2008.
- [84] Zhenda Lu, Chunguang Li, and Yadong Yin. "Synthesis and thermochromic properties of vanadium dioxide colloidal particles". In: *Journal of Materials Chemistry* 21.38 (2011), p. 14776. DOI: [10.1039/c1jm12430g](https://doi.org/10.1039/c1jm12430g).
- [85] J. Y. Suh et al. "Semiconductor to metal phase transition in the nucleation and growth of VO<sub>2</sub> nanoparticles and thin films". In: *Journal of Applied Physics* 96.2 (2004), pp. 1209–1213. DOI: [10.1063/1.1762995](https://doi.org/10.1063/1.1762995).
- [86] K. M. Niang et al. "Microstructure scaling of metal-insulator transition properties of VO<sub>2</sub> films". In: *Applied Physics Letters* 118.12 (2021), p. 121901. DOI: [10.1063/5.0039607](https://doi.org/10.1063/5.0039607).
- [87] Y. Muraoka and Z. Hiroi. "Metal-insulator transition of VO<sub>2</sub> thin films grown on TiO<sub>2</sub> (001) and (110) substrates". In: *Applied Physics Letters* 80.4 (2002), pp. 583–585. DOI: [10.1063/1.1446215](https://doi.org/10.1063/1.1446215).

- [88] Yuanbao Li et al. "Effects of the annealing process on the structure and valence state of vanadium oxide thin films". In: *Materials Research Bulletin* 100 (2018), pp. 220–225. DOI: [10.1016/j.materresbull.2017.12.028](https://doi.org/10.1016/j.materresbull.2017.12.028).
- [89] A. L. Patterson. "The Scherrer formula for X-ray particle size determination". In: *Physical Review* 56.10 (1939), 978–982. DOI: [10.1103/physrev.56.978](https://doi.org/10.1103/physrev.56.978).
- [90] I. Kosta et al. "Influence of vanadium oxides nanoparticles on thermoelectric properties of an N-type mg<sub>2</sub>si<sub>0.888</sub>sn<sub>0.1</sub>sb<sub>0.012</sub> alloy". In: *Journal of Alloys and Compounds* 856 (2021), p. 158069. DOI: [10.1016/j.jallcom.2020.158069](https://doi.org/10.1016/j.jallcom.2020.158069).
- [91] H. Buhay et al. "Summary abstract: Reactive ion etching of vanadium dioxide thin films". In: *Journal of Vacuum Science and Technology A: Vacuum, Surfaces, and Films* 4.3 (1986), 440–442. DOI: [10.1116/1.573901](https://doi.org/10.1116/1.573901).
- [92] Taylor L. Mabe, James G. Ryan, and Jianjun Wei. "Functional thin films and nanostructures for sensors". In: *Fundamentals of Nanoparticles* (2018), 169–213. DOI: [10.1016/b978-0-323-51255-8.00007-0](https://doi.org/10.1016/b978-0-323-51255-8.00007-0).
- [93] Toon Coenen, Jorik van de Groep, and Albert Polman. "Resonant modes of single silicon nanocavities excited by electron irradiation". In: *ACS Nano* 7.2 (2013), 1689–1698. DOI: [10.1021/nn3056862](https://doi.org/10.1021/nn3056862).